CrossMark

Optimal design of periodic frame structures with negative thermal expansion via mixed integer programming

Masayuki Hirota · Yoshihiro Kanno

Abstract   When structures and microstructures consisting of two or more materials with positive thermal expansion have specific configurations, they are able to have negative thermal expansion coefficients, i.e., they contract when heated. This paper proposes a topology optimization methodology of frame structures for designing a planar periodic structure that exhibits negative thermal expansion property. Provided that beam section of each existing member is chosen from a set of finitely many predetermined candidates, we show that this topology optimization problem with multiple material phases can be formulated as a mixed-integer linear programming problem. A global optimal solution can hence be found with a readily available software package. Since the proposed method treats frame structures and addresses local stress constraints, the optimal solution contains neither thin members nor hinge-like regions. To avoid too complicated structural designs realized as assemblage of many small pieces, this paper develops the constraints that separate distributions of two different materials. Numerical experiments are performed to show that structures with negative or near zero thermal expansion can be obtained by the proposed method.

M. Hirota · Y. Kanno (✉)
Department of Mathematical Informatics, Graduate School of Information Science and Technology, University of Tokyo, Tokyo 113-8656, Japan
e-mail: kanno@mist.i.u-tokyo.ac.jp

Y. Kanno
Materials and Structures Laboratory, Tokyo Institute of Technology, Yokohama 226-8503, Japan

1 Introduction

There exist many engineering structures that undergo large thermal stresses due to large temperature changes. For instance, the surface of a hypersonic cruise vehicle may be above 1000 °C due to viscous heating, which makes crucial thermal expansion mismatch between the vehicle interior; see Steeves and Evans (2011) and the references therein. Ducted exhaust systems of engines of low-observable aircrafts are also subjected to very large thermal stresses (Deaton and Grandhi 2013). Other examples include aerospace structures subjected to non-uniform heating, such as satellite telescope structures (Jacquot et al. 1998) and lattice structures for supporting satellite antennae and photovoltaic arrays (Palumbo et al. 2011). These structures undergo large temperature differences between sunny and shady sides. In such a situation, materials and/or structures with (nearly) zero thermal expansion properties are attractive.

The majority of materials have positive thermal expansion coefficients. Materials with negative thermal expansion coefficients will contract when they are heated. Some materials, e.g., zirconium tungstate family (Sleight 1998; Ramirez and Kowach 1998; Martinek and Hummel 1968; Evans et al. 1999) and a number of zeolites (Lightfoot et al. 2001), have negative thermal expansion coefficients. Such materials might be used, together with conventional materials, to make composites that have any desired thermal expansion properties. As another application, Sleight (1998) mentioned that sensitive temperature sensors can be made by combining thin films of materials with large positive and large negative thermal expansion properties. Thermal contraction property also has an application to thermal fasteners, which can be inserted into a hole at high temperature and fits tightly into the hole when it cools down (Sigmund and Torquato 1996). See Miller et al. (2009), Lind (2012), Barrera et al. (2005), Evans (1999), and Sleight (1998) for extensive surveys on negative thermal expansion solids.

Using two constituents with different positive thermal expansion coefficients, one can design three-phase materials, i.e., composites of two constituents combined with empty spaces, so as to have overall negative thermal expansion coefficients (Lakes 1996; Gibiansky and Torquato 1997; Sigmund and Torquato 1997). Sigmund and Torquato (1996, 1997) actually found such designs of three-phase composites by solving three-phase topology optimization problems. Chen et al. (2001) also showed that microstructures with unusual thermoelastic properties can be found by using topology optimization. Subsequently, various types of negative thermal expansion composites, consisting of positive thermal expansion materials, have been proposed; e.g., sandwich composite structures (Grima et al. 2010), composites with needle-like inclusions (Grima et al. 2010), and the ones with disc and cylindrical shaped inclusions (Grima et al. 2013). Also, periodic lattice structures consisting of two positive thermal expansion materials have attracted much attention. Lakes (1996) and Jefferson et al. (2009) presented bi-material lattices that can exhibit negative thermal expansion properties. Grima et al. (2007) showed that a simple periodic truss structure consisting of three different materials can have wide range of positive and negative thermal expansion properties. Lim (2005, 2012) presented two-material periodic hinged structures that can exhibit negative thermal expansion. Steeves et al. (2007) designed two-material periodic lattice structures that have near-zero thermal expansion together

with high stiffness. Miller et al. (2008) performed tailoring thermal expansion property of a three-bar truss, one member of which consists of a material different from the other two members. This unit triangle truss can be tessellated into more complex structures.

Many studies have been done concerning structural optimization under thermal loads. Thermal stress is a typical design-dependent load. As early works, Rodrigues and Fernandes (1995) developed homogenization method for topology optimization of thermoelastic structures and Jog (1996) treated material and geometrical nonlinearity. Topology optimization has been used to design thermally actuated compliant mechanisms (Li et al. 2004; Sigmund 2001). Recent studies on optimization of thermoelastic structures include Pedersen and Pedersen (2010, 2012), Deaton and Grandhi (2013), Wang et al. (2011), Gao and Zhang (2010), Deng et al. (2013), and Xia and Wang (2008). Among them, Pedersen and Pedersen (2010) discussed that, for maximizing strength of thermoelastic structures, minimization of compliance is questionable and attempted to find a design with uniform energy density. Deng et al. (2013) optimized an overall thermoelastic structure and its material microstructure simultaneously.

There might exist some links between negative thermal expansion and negative Poisson's ratio properties; see, e.g., Lim (2005), Grima et al. (2010), Baughman and Galvão (1993), and Miller et al. (2008). Recently Kureta and Kanno (2014) proposed a topology optimization method of frame structures to design a periodic planar structure that exhibits negative Poisson's ratio property. In this method, the optimization problem is recast as a *mixed-integer linear programming* (MILP) problem and is solved globally. The optimal solution has neither hinges nor thin members and local stress constraints were fully addressed in optimization. The computed optimal solution was actually fabricated by applying a photo-etching technique to a steel plate. It was confirmed that the fabricated model actually exhibits negative Poisson's ratio property. In continuation of this previous work, the present paper develops an MILP approach to designing a planar periodic frame structure that exhibits negative thermal expansion property. We suppose that a periodic frame structure is constructed by connecting a unique base cell, i.e., the smallest unit, and that each member of the frame structure consists of either one of given two different positive thermal expansion materials or void. Based upon the conventional ground structure method, topology of the base cell is optimized to minimize its thermal expansion coefficient. Material selection for each member, from among the two materials and void, is handled directly by using discrete design variables. Local stress constraints are imposed on existing members. Small deformation is assumed throughout the paper and issues of material and geometrical nonlinearity are not addressed. A global optimal solution is then found with an existing algorithm for MILP; several software packages, e.g., CPLEX (IBM ILOG 2013), are available for this purpose. The MILP formulation presented in this paper is viewed as a natural extension of the one for frame optimization proposed by Kureta and Kanno (2014). Similar MILP formulations for structural optimization were developed for continua with binary design variables (Stolpe and Svanberg 2003; Stolpe 2007), trusses with discrete member cross-sectional areas (Rasmussen and Stolpe 2008), and tensegrity structures (Kanno 2013).

Continuum topology optimization for achieving negative thermal expansion property sometimes results in very complicated structural designs. Also, the

obtained structures often have hinge-like regions. Such designs may in practice require manual post-processing before actual fabrication process. For instance, Qi and Halloran (2004) used a microfabrication by an oxide co-extrusion technique to fabricate the optimal design obtained by Chen et al. (2001) and mentioned that "an engineering interpretation of the theoretical design" was necessary for strengthening some weak parts and smoothing material distribution. It is actually often that optimal solutions, obtained by continuum topology optimization, have hinge-like regions, because hinges help thermal contraction deformation to attain extremum. Thickness of hinges of an optimal solution should be adjusted carefully before fabrication process, because a structure with thin hinges can sustain only small forces while by thickening hinges the structure may lose basic feature from which negative thermal expansion accrues. One possible remedy for this issue might be to use a special technique to avoid hinge-like regions; hinge-free optimization is a current active research topic in continuum topology optimization (Poulsen 2003; Sigmund 2007; Yoon et al. 2004; Zhu et al. 2013). Alternatively, this paper proposes to use topology optimization of frame structures. In our approach, local stress constraints are fully addressed in the optimization process. Also, the section of each member is chosen from predetermined candidates. Consequently, the optimal solution has neither hinges nor thin members and, hence, may be able to be fabricated without manual post-processing, like the one with negative Poisson's ratio obtained in the previous work (Kureta and Kanno 2014). It should be mentioned that topology optimization of continuum structures with local stress constraints have been a challenging problem and various approaches are still being examined; see, e.g., Duysinx (1998), Cheng and Guo (1997), Bruggi (2008), Allaire and Jouve (2008), Guo et al. (2011), Holmberg et al. (2013), and references therein. Most of existing studies on local stress constraints consider single-material phase topology optimization problems.

The paper is organized as follows. Section 2 design presents a concept of design problem of a periodic frame structure exhibiting negative thermal expansion behavior. Section 3 recasts this design problem as an MILP. Section 4 develops an alternative formulation to obtain a base cell such that the distributions of the two different materials are clearly separated. Section 5 presents numerical experiments. We conclude in Sect. 6.

2 Design problem of structures with negative thermal expansion

Section 2.1 defines a design problem of a planar periodic frame structure with negative thermal expansion coefficient property. Section 2.2 formulates an optimization problem of a base cell frame structure, where structural topology and material distribution are simultaneously optimized.

2.1 Periodic frame structure with thermal contraction

We consider a planar frame structure realized by arranging a basic frame unit repeatedly. The properties of this frame structure are described as follows.

© Springer

(i)   The structure has periodicity such that a unique base cell, i.e., the smallest square unit, is connected repeatedly in a regular way.

(ii)   As for connection pattern of base cells, we consider two cases in Fig. 1. In the case of pattern (A), we add four short beams to a base cell as shown in Fig. 1a, in order to connect the cell to adjacent ones. In the case of pattern (B) in Fig. 1b, the nodes at the four corners of the base cell serve as interfaces for connection.

(iii) Thermal deformation of the base cell is supposed to have square symmetry.

(iv)   The whole periodic structure consisting of the base cells will contract when temperature is elevated from the ordinary value.

The design domain of our design problem is the base cell shown in Fig. 2a, due to the periodicity property in (i). To realize the symmetry property in (iii), we suppose that the configuration of the unit cell is symmetric with respect to reflection across the thin lines in Fig. 2a. Figure 2b shows an example of ground structure, which corresponds to a quarter of the base cell in Fig. 2a. The dashed line in Fig. 2b is an axis of symmetry of the structural design. Also, from property (iii), deformation of the whole periodic structure depends solely upon the displacements of the four nodes described in property (ii). We call these four nodes *interface nodes*. Property (iv) defines the negative thermal expansion property considered in this paper. This property can be related to the displacement of the interface node as follows. Suppose that base cells are connected according to pattern (A) in Fig. 1a. Let u_1 and u_2 denote the displacements of two interface nodes of the unit cell, as shown in Fig. 2b, when temperature increases by the specified degrees ΔT (> 0). The side length of a unit cell is l_{cell}. From property (iii), thermoelastic deformation is symmetric, and hence $u_1 = u_2$. Hence, the side length of the cell becomes $l_{\text{cell}} + 2u_1$ due to temperature elevation ΔT. The thermal coefficient of area expansion, which is given by the ratio of the area occupied by the deformed cell to the undeformed area, is written as
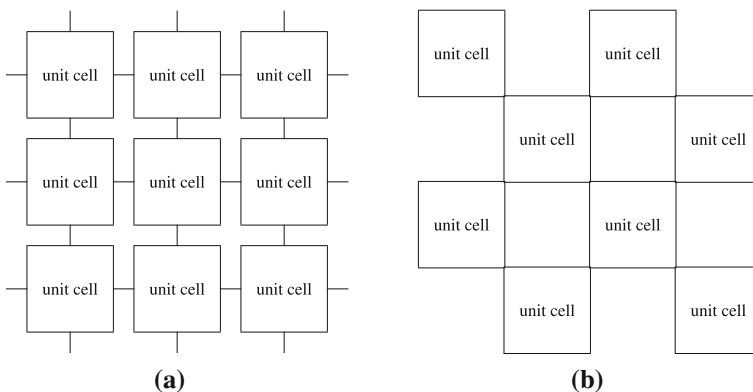

Fig. 1 Two types of repeated frame structures obtained by connecting unit base cells. **a** Connection pattern (A); and **b** connection pattern (B)
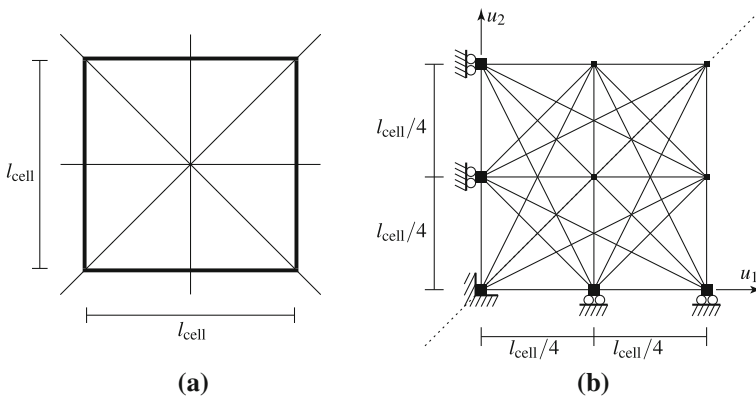
Fig. 2 Problem setting. **a** A unit base cell and symmetry axes; and **b** an example of ground structure

$$\frac{(l_{\text{cell}} + 2u_1)^2}{l_{\text{cell}}^2} \simeq 1 + \frac{4u_1}{l_{\text{cell}}}.$$

Therefore, the structure shows thermal contraction if the interface nodes of the base cell move inward from their positions at the ordinary temperature. This motivates us to minimize $u_1 \, (= u_2)$ at the equilibrium state under temperature elevation ΔT. Similarly, for connection pattern (B), we can consider a minimization problem of a displacement of a corner node of the base cell.

In designing a base cell, we explore the structure with a minimum thermal expansion coefficient by making use of some different materials with positive thermal expansion coefficients. More precisely, we determine the material that constitutes each member of the ground structure. Members will be removed if the null material is assigned. Thus we simultaneously optimize topology and material distribution of the base cell. In the course of optimization we shall make use of the following assumptions.

– Small deformations and linear elasticity are assumed.
– The base cell is supposed to consist of two different materials with positive thermal exposition coefficients.[1] Each member is thereby to be assigned either material 1, material 2, or void. Material parameters of these two materials are specified a priori.
– At nodes of the frame structure, members constituted different materials are assumed to be bonded perfectly.
– Temperature is assumed to distribute uniformly in the frame structure.
– In the thermal deformation of each beam element, the axial extension is dominant and expansions in the other directions are assumed to be negligible.

---

[1] Extension of the proposed formulation to a case with more than two materials is straightforward; see Remark 7.

Thus the problem dealt with in this paper is viewed as a three-phase (i.e., two materials and void) material distribution optimization on a given ground structure. For continuum structures, three-phase topology optimization has been studied extensively; see, e.g., Chen and Kikuchi (2001), Chen et al. (2001), and Sigmund and Torquato (1997).

As observed in Sigmund and Torquato (1997), it is often that structures with negative thermal expansion coefficients have low global stiffness. An example is, as discussed in Steeves et al. (2007), a bi-material lattice due to Lakes (1996). For practical applications, we therefore introduce the constraint on the global stiffness in the course of optimization. Specifically, we suppose that fictitious external forces are applied to the interface nodes at the ordinary temperature as shown in Fig. 3 and impose the upper bound constraint for the compliance, together with the local stress constraints. Pedersen and Pedersen (2010) pointed out that, for thermoelastic structures, minimization of compliance does not necessarily result in a design with maximum strength. In this paper we consider local stress constraints, both at the elevated and ordinary temperatures, for securing structural strength directly.

Descriptive summary of the optimization problem considered in this paper is given as follows.

- Topology optimization problem of a planar frame structure is solved to obtain a base cell. Selection of materials, including the null material, for each beam element is considered a design variable. The material parameters of the constituent materials are specified.
- The displacement of the interface node induced by the temperature increase is minimized.
- The section of each existing beam element is specified.[2]
- Compliance constraint is considered for the external forces applied to the interface nodes.
- Stress constraints of existing beam elements are fully addressed.
- Existence of mutually crossing beam elements is not allowed.

In the optimization process, selection of constituent materials is handled by using some discrete design variables. We solve the optimization problem within the framework of mixed integer programming. Usually, in topology optimization of continua, material selection is handled with an interpolation and penalization scheme of material constants. As an extension of the standard SIMP (solid isotropic material with penalization) scheme for interpolation, Sigmund and Torquato (1997) and Gibiansky and Sigmund (2000) presented a three-phase (i.e., two materials and void) topology optimization method. In this method, two variables are used for each finite element, where one of them determines whether the element is void or not and the other interpolates the material constants of the two constituent materials. This interpolation scheme was further extended to optimization with arbitrary many materials by Stegmann and Lund (2005). An extension of the RAMP (rational

---

[2] Extension of the proposed formulation to a case with more than one available beam sections is straightforward; see Remark 1.
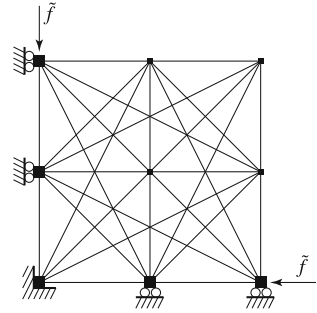
approximation of material properties) scheme to multiple material phases is due to Hvejsel and Lund (2011). Bruyneel (2011) proposed to use shape functions of finite element method to represent the weights in material interpolation. Multi-material topology optimization was also treated within the frameworks of level-set methods (Wang and Wang 2004) and phase-field methods (Zhou and Wang 2007). For instance, in the multi-phase level-set method due to Wang and Wang (2004), one material domain is represented as a union of level sets of some different implicit functions. In contrast to the literature cited above, the approach presented in this paper does not resort to any interpolation or penalization techniques but directly solves an optimization problem with discrete design variables. Since the optimization problem is recast as an MILP, a global optimal solution can be found by using, e.g., a branch-and-cut method. This guaranteed global optimality might be considered a major advantage of the proposed method to the existing methods using interpolation and penalization. Instead, a potential disadvantage of the proposed method is that computational cost to solve the optimization problem might increase drastically as the number of discrete design variables increases. This is because algorithms for MILP are essentially based on enumeration of solutions.

Remark 1 Suppose that section of each member of the base cell is chosen from a set of some (i.e., finitely many) predetermined candidates. Then the design optimization problem can still be formulated as an MILP. For simplicity of presentation, however, this paper discusses only the case where single candidate is given for each member. Extension to the case with more than one candidate sections can be done in a manner similar to Kureta and Kanno (2014).

2.2 Optimization problem

This section presents the optimization problem for the design problem sketched in Sect. 2.1.

Consider a planar frame structure that serves as a ground structure. Figure 2b shows an example. The ground structure consists of many candidate members. Each member is modeled as a Timoshenko beam element. Locations of nodes are specified. Let $\mathcal{E}$ and $\mathcal{V}$ denote the set of members and the set of nodes, respectively.

For example, the ground structure in Fig. 2b consists of $|\mathcal{E}| = 28$ members and $|\mathcal{V}| = 9$ nodes.

Suppose that the material of each member is chosen among "material 1" and "material 2." Let $\mathcal{M}_1$ and $\mathcal{M}_2$ denote the sets of members constituted by material 1 and material 2, respectively. We use $\mathcal{N}$ to denote the set of members removed as a result of optimization. Then the design problem is regarded as a problem finding a partition

$$\mathcal{E} = \mathcal{M}_1 \cup \mathcal{M}_2 \cup \mathcal{N} \qquad (1)$$

of $\mathcal{E}$, where $\mathcal{M}_1, \mathcal{M}_2$, and $\mathcal{N}$ are disjoint sets. Material parameters of the constituent materials, listed in Table 1, are specified.

As discussed in Sect. 2.1, we attempt to minimize the target displacement induced by the temperature increase to find the structure with the minimum thermal expansion behavior. Consider the equilibrium state of the frame structure when increase in temperature of ΔT degrees is given. Let $\boldsymbol{u} \in \mathbb{R}^d$ denote the vector of nodal displacements, where d is the number of degree of freedom of displacements. It should be clear that $\boldsymbol{u} = \boldsymbol{0}$ when no external load is applied at the ordinary temperature. For member $e \in \mathcal{E}$, let E_e, G_e, and α_e denote the Young modulus, shear modulus, and thermal expansion coefficient, respectively. For notational convenience, we use vectors $\boldsymbol{E} = (E_e \mid e \in \mathcal{E}), \boldsymbol{G} = (G_e \mid e \in \mathcal{E})$, and $\boldsymbol{\alpha} = (\alpha_e \mid e \in \mathcal{E})$. We use $K(\boldsymbol{E}, \boldsymbol{G}) \in \mathbb{R}^{d \times d}$ to denote the stiffness matrix. The equation of thermoelastic equilibrium may be written as

$$K(\boldsymbol{E}, \boldsymbol{G})\boldsymbol{u} - \boldsymbol{t}(\boldsymbol{\alpha}, \Delta T) = \boldsymbol{0}, \qquad (2)$$

where $\boldsymbol{t}(\boldsymbol{\alpha}, \Delta T) \in \mathbb{R}^d$ is the vector of thermal forces. Explicit expression of (2) will be presented in Sect. 3.1. Thus we attempt to minimize u_1 in Fig. 2b under constraint (2). Here, it should be clear that E_e, G_e, and α_e depend on selection of the material that constitutes member e. Precisely, we have that $E_e = \bar{E}_1$ if $e \in \mathcal{M}_1, E_e = \bar{E}_2$ if $e \in \mathcal{M}_2$, and $E_e = 0$ if $e \in \mathcal{N}$. In the same manner, G_e and α_e are treated as discrete design variables.

The sections of existing members ($e \notin \mathcal{N}$) are specified a priori. Let $\bar{A}, \bar{I}$, and $\bar{Z}$ denote the specified cross-sectional area, moment of inertia, and elastic section modulus, respectively. We use κ to denote the shear correction factor in the Timoshenko beam theory. These parameters are treated as constants in the optimization problem.

We next consider the compliance constraint. Without taking into account the global stiffness of the structure, the topology optimization problem that minimizes

Table 1 The material parameters of the constituent materials	Material parameter	$\mathcal{M}_1$	$\mathcal{M}_2$	$\mathcal{N}$
	Young's modulus	$\bar{E}_1$	$\bar{E}_2$	0
	Shear modulus	$\bar{G}_1$	$\bar{G}_2$	0
	Thermal expansion coefficient	$\bar{\alpha}_1$	$\bar{\alpha}_2$	0
	Yield stress	$\bar{\sigma}_1^{\mathrm{y}}$	$\bar{\sigma}_2^{\mathrm{y}}$	0

the target displacement has meaningless optimal solutions. As an extreme example, if all the members of the ground structure vanish, then the target node can move freely. Such a solution is optimal and, hence, the optimal value is not bounded below. To make the optimization problem meaningful, we use the upper bound constraint of the compliance. Suppose that, at the ordinary temperature, external forces are applied to the interface nodes as shown in Fig. 3. We use $\tilde{\boldsymbol{f}} \in \mathbb{R}^d$ to denote this external load. The displacement vector, $\tilde{\boldsymbol{u}} \in \mathbb{R}^d$, at the equilibrium state in the presence of $\tilde{\boldsymbol{f}}$ is obtained from

$$K(\boldsymbol{E}, \boldsymbol{G})\tilde{\boldsymbol{u}} = \tilde{\boldsymbol{f}}. \tag{3}$$

It should be clear that $\tilde{\boldsymbol{u}}$ is different from the solution, $\boldsymbol{u}$, of (2); the latter is the displacement induced by the thermal change when no external force is applied. The compliance constraint is then written as

$$\tilde{\boldsymbol{f}}^{\top}\tilde{\boldsymbol{u}} \leq c^{\mathrm{u}}, \tag{4}$$

where $c^{\mathrm{u}} > 0$ is the specified upper bound.

Stress constraints are formulated as follows. Consider member $e = (i,j) \in \mathcal{E}$, which connects node i and node j $(i,j \in \mathcal{V})$. Let $m_e^{(i)}$ and $m_e^{(j)}$ denote the two end moments. We use q_e to denote the axial force. Since members are subjected to nodal loads only, the stress constraints are considered only at the two ends of member e. Based upon a simple piecewise-linear model of yield condition, stress constraint can be written as

$$\frac{|q_e|}{\bar{A}} + \frac{\max\left\{|m_e^{(i)}|, |m_e^{(j)}|\right\}}{\bar{Z}} \leq \sigma_e^{\mathrm{u}}. \tag{5}$$

The upper bound for stress, σ_e^{u}, depends on the material constituting member e as

$$\sigma_e^{\mathrm{u}} = \begin{cases} \bar{\sigma}_1^{\mathrm{u}} & \text{if } e \in \mathcal{M}_1, \\ \bar{\sigma}_2^{\mathrm{u}} & \text{if } e \in \mathcal{M}_2, \\ 0 & \text{if } e \in \mathcal{N}, \end{cases} \tag{6}$$

where $\bar{\sigma}_1^{\mathrm{u}}$ and $\bar{\sigma}_2^{\mathrm{u}}$ are positive constants.[3] For notational convenience, define $\varphi : \mathbb{R}^3 \to \mathbb{R}$ by

$$\begin{aligned} \varphi(q_e, m_e^{(i)}, m_e^{(j)}) &= \frac{|q_e|}{\bar{A}} + \frac{\max\left\{|m_e^{(i)}|, |m_e^{(j)}|\right\}}{\bar{Z}} \\ &= \frac{|q_e|}{\bar{A}} + \frac{1}{2}\frac{|m_e^{(i)} + m_e^{(j)}|}{\bar{Z}} + \frac{1}{2}\frac{|m_e^{(i)} - m_e^{(j)}|}{\bar{Z}}. \end{aligned} \tag{7}$$

Then (5) is written as

---

[3] For example, we may determine $\bar{\sigma}_1^{\mathrm{u}}$ and $\bar{\sigma}_2^{\mathrm{u}}$ from the yield stresses of the materials and a safety factor; see Remark 2.

$$\varphi(q_e, m_e^{(i)}, m_e^{(j)}) \leq \sigma_e^{\mathrm{u}}. \tag{8}$$

Presence of mutually crossing members should be avoided. Let $\mathcal{E}_{\mathrm{cross}}$ denote the set of pairs of members that mutually cross in the ground structure. Namely, we write $(e, e') \in \mathcal{E}_{\mathrm{cross}}$ if member e and member e' cross. Then at least one of these two members should belong to $\mathcal{N}$. This condition is further equivalent to

$$\{e, e'\} \not\subseteq \mathcal{M}_1 \cup \mathcal{M}_2, \quad \forall (e, e') \in \mathcal{E}_{\mathrm{cross}}.$$

By summing up the results in this section, the optimization problem to be solved is formulated as follows.

$$\min \quad u_1 \tag{9a}$$

$$\mathrm{s.\,t.} \quad K(E, G)u - t(\alpha, \Delta T) = \mathbf{0}, \tag{9b}$$

$$\varphi(q_e(u), m_e^{(i)}(u), m_e^{(j)}(u)) \leq \sigma_e^{\mathrm{u}}, \qquad\qquad \forall e = (i, j) \in \mathcal{E}, \tag{9c}$$

$$K(E, G)\tilde{u} = \tilde{f}, \tag{9d}$$

$$\tilde{f}^{\top} \tilde{u} \leq c^{\mathrm{u}}, \tag{9e}$$

$$\varphi(q_e(\tilde{u}), m_e^{(i)}(\tilde{u}), m_e^{(j)}(\tilde{u})) \leq \sigma_e^{\mathrm{u}}, \qquad\qquad \forall e = (i, j) \in \mathcal{E}, \tag{9f}$$

$$\{e, e'\} \not\subseteq \mathcal{M}_1 \cup \mathcal{M}_2, \quad \forall (e, e') \in \mathcal{E}_{\mathrm{cross}}, \tag{9g}$$

$$(\alpha_e, E_e, G_e, \sigma_e^{\mathrm{u}}) = \begin{cases} (\bar{\alpha}_1, \bar{E}_1, \bar{G}_1, \bar{\sigma}_1^{\mathrm{u}}) & \text{if } e \in \mathcal{M}_1, \\ (\bar{\alpha}_2, \bar{E}_2, \bar{G}_2, \bar{\sigma}_2^{\mathrm{u}}) & \text{if } e \in \mathcal{M}_2, \quad \forall e \in \mathcal{E}. \\ (0, 0, 0, 0) & \text{if } e \in \mathcal{N}, \end{cases} \tag{9h}$$

Here, the decision variables in optimization are $u, \tilde{u}, \mathcal{M}_1, \mathcal{M}_2$, and $\mathcal{N}$. We select the constituent material of each member according to (9h), where $\{\mathcal{M}_1, \mathcal{M}_2, \mathcal{N}\}$ is a partition of $\mathcal{E}$. Constraints (9b) and (9c) are concerned with the equilibrium state at the high temperature, and thence the minimal thermal expansion property is achieved by minimizing u_1. Constraints (9d), (9e), and (9f) are concerned with the equilibrium state at the ordinary temperature, where the fictitious external load, $\tilde{f}$, is applied. Constraints on the compliance and member stresses are considered. Presence of mutually crossing members is forbidden by (9g).

Remark 2 Stress constraint (5) has been derived as follows. Let $\bar{\sigma}_p^{\mathrm{y}}$ denote the yield stress of material p ($p = 1, 2$), which is a given constant. The upper bound stress, $\bar{\sigma}_p^{\mathrm{u}}$, may be determined as

$$\bar{\sigma}_p^{\mathrm{u}} = \bar{\sigma}_p^{\mathrm{y}} / \gamma,$$

where $\gamma \geq 1$ is a specified safety factor. Then the upper bound stress of member

$e = (i, j)$ is defined by (6). The upper bounds for absolute values of the axial force and the end moment, denoted q_e^{u} and m_e^{u}, are given by

$$q_e^{\mathrm{u}} = \sigma_e^{\mathrm{u}} \bar{A}, \quad m_e^{\mathrm{u}} = \sigma_e^{\mathrm{u}} \bar{Z}. \tag{10}$$

The stress constraints are written at both ends of the member as

$$\frac{|q_e|}{q_e^{\mathrm{u}}} + \frac{|m_e^{(i)}|}{m_e^{\mathrm{u}}} \le 1, \quad \frac{|q_e|}{q_e^{\mathrm{u}}} + \frac{|m_e^{(j)}|}{m_e^{\mathrm{u}}} \le 1. \tag{11}$$

By substituting (10) into (11) and putting together the two inequalities, we obtain (5).

Remark 3 Generally speaking, in topology optimization the stress constraints should be imposed only on existing members. In other words, if member e vanishes in the course of optimization, i.e., if $e \in \mathcal{N}$, then the stress constraint on member e should be removed from the optimization problem (Cheng and Guo 1997; Achtziger and Kanzow 2008; Rozvany 2001). It should be clear that in this section the stress constraints, i.e., (9c) and (9f), have been formulated in terms of the axial force and the two end moments. In the course optimization, all the members have a specified common section, i.e., $\bar{A}, \bar{I}$, and $\bar{Z}$ are considered constants, while the material parameters for $e \in \mathcal{N}$ are $\alpha_e = E_e = G_e = 0$. Therefore, if $e = (i, j) \in \mathcal{N}$, then we obtain

$$q_e(\boldsymbol{u}) = m_e^{(i)}(\boldsymbol{u}) = m_e^{(j)}(\boldsymbol{u}) = 0.$$

This implies that adding the condition

$$\varphi(q_e, m_e^{(i)}, m_e^{(j)}) \le 0, \quad \forall e \in \mathcal{N} \tag{12}$$

to the optimization problem as the constraints does not change the feasible set. Condition (12) has been actually incorporated in (9c) and (9f).

Remark 4 As explained in Sect. 2.1, the configuration of the unit cell is set to be symmetric with respect to the dashed line in Fig. 2b. This constraint is formally written as follows. Let $\mathcal{E}_{\mathrm{sym}}$ denote the set of pairs of members that are located at symmetric positions. Namely, we write $(e, e') \in \mathcal{E}_{\mathrm{sym}}$ if member e is swapped with member e' by the reflection depicted in Fig. 2b. Then these two members should have the same material selection, i.e., each $(e, e') \in \mathcal{E}_{\mathrm{sym}}$ should satisfy

$$e \in \mathcal{M}_1 \quad \Leftrightarrow \quad e' \in \mathcal{M}_1, \tag{13a}$$

$$e \in \mathcal{M}_2 \quad \Leftrightarrow \quad e' \in \mathcal{M}_2, \tag{13b}$$

$$e \in \mathcal{N} \quad \Leftrightarrow \quad e' \in \mathcal{N}. \tag{13c}$$

In practice, this condition is added to problem (9) as a constraint.

3 Mixed-integer linear programming approach

In this section we present an MILP approach to the design optimization problem for finding frame structures with negative thermal expansion properties. As mentioned in Sect. 2.2, in this design problem each member belongs either $\mathcal{M}_1$, $\mathcal{M}_2$, or $\mathcal{N}$. We express this choice by making use of two 0–1 design variables. Section 3.1 presents explicit forms of the constraints of problem (9). Section 3.2 reformulates problem (9) as an MILP problem.

3.1 Thermoelastic equilibrium equations with material selection

In this section we write the constraints of problem (9) explicitly as preparation for the MILP formulation presented in Sect. 3.2. Particular attention is focused on the thermoelastic equilibrium equation, (9b), in conjunction with the material selection constraint, (9h). A key is the decomposition of the stiffness matrix of a frame structure, which was used also in Kureta and Kanno (2014). Two differences from the previous formulation in Kureta and Kanno (2014) are that we now consider thermal effect and material selection.

According to Sect. 3.2 of Kureta and Kanno (2014), the equilibrium equation,

$$K(E, G)u = f, \tag{14}$$

is decomposed into the force-balance equation written as

$$\sum_{e \in \mathcal{E}} \sum_{t=1}^{3} s_{et} \boldsymbol{b}_{et} = \boldsymbol{f} \tag{15}$$

and the relations between the generalized stresses and the displacement vector written as

$$s_{et} = k_{et} \boldsymbol{b}_{et}^{\top} \boldsymbol{u}, \quad t = 1, 2, 3; \ \forall e \in \mathcal{E}. \tag{16}$$

Here, $\boldsymbol{b}_{e1}, \boldsymbol{b}_{e2}, \boldsymbol{b}_{e3} \in \mathbb{R}^d \ (\forall e \in \mathcal{E})$ are constant vectors. Constants $k_{e1}, k_{e2}, k_{e3} \in \mathbb{R} \ (\forall e \in \mathcal{E})$ are defined by

$$k_{e1} = \frac{E_e A_e}{l_e}, \tag{17a}$$

$$k_{e2} = \frac{1}{l_e} \left(\frac{l_e^2}{12 E_e I_e} + \frac{1}{\kappa G_e A_e} \right)^{-1}, \tag{17b}$$

$$k_{e3} = \frac{E_e I_e}{l_e}, \tag{17c}$$

where A_e is the cross-sectional area, I_e is the moment of inertia, and l_e is the undeformed length of beam element e. In (17b), we define $k_{e2} = 0$ if $E_e = G_e = 0$ for convention. By eliminating s_{et}'s, we see that (15) and (16) revert to (14).

Expression in (15) and (16) serves as basis of our MILP formulation. Details of the decomposition above appear in appendix 7.

The equation of thermoelastic equilibrium, (2), can be written explicitly as follows. Let l_e denote the undeformed length of member e ($e \in \mathcal{E}$). Due to temperature change ΔT, the length of the member becomes $l_e(1 + \alpha_e \Delta T)$. Therefore, the relation between the axial force and the displacements, i.e., $t = 1$ in (16), is now given by

$$s_{e1} = k_{e1}(\boldsymbol{b}_{e1}^\top \boldsymbol{u}_e - l_e \alpha_e \Delta T).$$

Since we assume that thermal expansions in directions other than the axial direction are negligible, s_{e2} and s_{e3} are given by (16). Recall that, in the course of optimization, coefficients k_{e1}, k_{e2}, k_{e3}, and α_e are determined by the material selected for member e. By incorporating this selection, we see that the equation of thermoelastic equilibrium can be written explicitly as

$$\sum_{e \in \mathcal{E}} \sum_{t=1}^{3} s_{et} \boldsymbol{b}_{et} = \boldsymbol{0}, \tag{18a}$$

$$s_{e1} = \begin{cases} \bar{k}_{e11}(\boldsymbol{b}_{e1}^\top \boldsymbol{u} - l_e \bar{\alpha}_1 \Delta T) & \text{if } e \in \mathcal{M}_1, \\ \bar{k}_{e12}(\boldsymbol{b}_{e1}^\top \boldsymbol{u} - l_e \bar{\alpha}_2 \Delta T) & \text{if } e \in \mathcal{M}_2, \\ 0 & \text{if } e \in \mathcal{N}, \end{cases} \tag{18b}$$

$$s_{et} = \begin{cases} \bar{k}_{et1} \boldsymbol{b}_{et}^\top \boldsymbol{u} & \text{if } e \in \mathcal{M}_1, \\ \bar{k}_{et2} \boldsymbol{b}_{et}^\top \boldsymbol{u} & \text{if } e \in \mathcal{M}_2, \quad t = 2, 3, \\ 0 & \text{if } e \in \mathcal{N}, \end{cases} \tag{18c}$$

where constants $\bar{k}_{etp}$ ($t = 1, 2, 3; \ p = 1, 2$) are defined by

$$\bar{k}_{e1p} = \frac{\bar{E}_p \bar{A}}{l_e}, \tag{19a}$$

$$\bar{k}_{e2p} = \frac{1}{l_e} \left(\frac{l_e^2}{12 \bar{E}_p \bar{I}} + \frac{1}{\bar{G}_p \kappa A} \right)^{-1}, \tag{19b}$$

$$\bar{k}_{e3p} = \frac{\bar{E}_p \bar{I}}{l_e}. \tag{19c}$$

The displacement in the compliance constraint, (9e), is defined by the equilibrium equation at the ordinary temperature, (9d). By using expression in (15) and (16), (9d) can be rewritten as

$$\sum_{e \in \mathcal{E}} \sum_{t=1}^{3} \tilde{s}_{et} \boldsymbol{b}_{et} = \tilde{\boldsymbol{f}}, \tag{20a}$$

$$\tilde{s}_{et} = k_{et} \boldsymbol{b}_{et}^\top \tilde{\boldsymbol{u}}, \quad t = 1, 2, 3; \ e \in \mathcal{E}, \tag{20b}$$

where $k_{et} = \bar{k}_{etp}$ if $e \in \mathcal{M}_p$, otherwise $k_{et} = 0$, as explicitly written in (18).

It is useful to rewrite the stress constraints, i.e., (9c) and (9f), in terms of the generalized stresses, s_{et} $(t = 1, 2, 3)$. It follows from (7) and (48) (in appendix 7) that (9c) can be rewritten as

$$\frac{|s_{e1}|}{\bar{A}} + \frac{1}{2}\frac{l_e|s_{e2}|}{\bar{Z}} + \frac{|s_{e3}|}{\bar{Z}} \leq \sigma_e^{\mathrm{u}}. \tag{21}$$

Similarly, (9f) can be rewritten as

$$\frac{|\tilde{s}_{e1}|}{\bar{A}} + \frac{1}{2}\frac{l_e|\tilde{s}_{e2}|}{\bar{Z}} + \frac{|\tilde{s}_{e3}|}{\bar{Z}} \leq \sigma_e^{\mathrm{u}}. \tag{22}$$

It should be clear that σ_e^{u} in (21) and (22) depends on material selection for member e; see (6).

As the upshot of this section, it is worth noting that constraints (18b), (18c), (20b), (21), and (22) involve terms depending on material selections. This reflects intrinsical combinatorial properties of our design problem. In Sect. 3.2 we shall introduce some binary variables to treat these constraints within the framework of MILP.

3.2 Reformulation to mixed-integer linear programming problem

In this section, optimization problem (9) presented in Sect. 2.2 is reduced to an MILP problem. We make use of the formulations developed in Sect. 3.1 for thermoelastic equilibrium equations.

As mentioned earlier, the design problem is interpreted as finding a partition of a set of members, (1), such that the objective function is minimized. A key idea to deal with this partition in our optimization problem is making use of integer variables that serve as labels of members. Specifically, we use two 0-1 variables,

$$(x_{e1}, x_{e2}) \in \{0, 1\}^2, \tag{23}$$

to express the label of member $e \in \mathcal{E}$ as

$$(x_{e1}, x_{e2}) = (1, 0) \quad \Leftrightarrow \quad e \in \mathcal{M}_1, \tag{24a}$$

$$(x_{e1}, x_{e2}) = (0, 1) \quad \Leftrightarrow \quad e \in \mathcal{M}_2, \tag{24b}$$

$$(x_{e1}, x_{e2}) = (0, 0) \quad \Leftrightarrow \quad e \in \mathcal{N}. \tag{24c}$$

These variables are subjected to the constraint

$$x_{e1} + x_{e2} \leq 1. \tag{25}$$

We begin by reformulating constraint (18), i.e., the equilibrium equation at the high temperature. Since (18a) is a linear constraint, attention is focused on (18b) and (18c). By making use of x_{e1} and x_{e2} in (24), (18b) can be rewritten as

$$|s_{e1} - \bar{k}_{e1p}(\boldsymbol{b}_{e1}^{\top}\boldsymbol{u} - l_e\bar{\alpha}_p\Delta T)| \leq L(1 - x_{ep}), \quad p = 1, 2, \tag{26a}$$

$$|s_{e1}| \leq L(x_{e1} + x_{e2}), \tag{26b}$$

where $L \gg 0$ is a sufficiently large constant. Similarly, (18c) is equivalent to

$$|s_{et} - \bar{k}_{etp}(\boldsymbol{b}_{et}^\top \boldsymbol{u})| \le L(1 - x_{ep}), \quad p = 1, 2; \quad t = 2, 3, \tag{27a}$$

$$|s_{et}| \le L(x_{e1} + x_{e2}), \qquad t = 2, 3. \tag{27b}$$

We next consider the stress constraint, (21). Note that σ_e^{u} in (21) is defined by (6), i.e.,

$$\sigma_e^{\mathrm{u}} = \bar{\sigma}_1^{\mathrm{u}} x_{e1} + \bar{\sigma}_2^{\mathrm{u}} x_{e2}.$$

Hence, (21) is equivalent to

$$\frac{|s_{e1}|}{\bar{A}} + \frac{l_e |s_{e2}|}{2\bar{Z}} + \frac{|s_{e3}|}{\bar{Z}} \le \bar{\sigma}_1^{\mathrm{u}} x_{e1} + \bar{\sigma}_2^{\mathrm{u}} x_{e2}. \tag{28}$$

Constraint (22) can be rewritten by using x_{e1} and x_{e2} similarly. By imposing (28) on the optimization problem as a constraint, constraints (26b) and (27b) become redundant and, thence, are omitted.

Constraint (9g), which avoids existence of mutually intersecting members, can also be written in terms of x_{e1} and x_{e2}. Observe that $x_{e1} + x_{e2} = 1$ holds if and only if $e \in \mathcal{M}_1 \cup \mathcal{M}_2$. Therefore, (9g) is equivalent to

$$x_{e1} + x_{e2} + x_{e'1} + x_{e'2} \le 1, \quad \forall (e, e') \in \mathcal{E}_{\mathrm{cross}}. \tag{29}$$

By summing up the results above, problem (9) is reduced to the following MILP problem:

$$\min \quad u_1 \tag{30a}$$

$$\mathrm{s.\,t.} \quad \sum_{e \in \mathcal{E}} \sum_{t=1}^{3} s_{et} \boldsymbol{b}_{et} = \boldsymbol{f}, \tag{30b}$$

$$|s_{e1} - \bar{k}_{e1p}(\boldsymbol{b}_{e1}^\top \boldsymbol{u} - l_e \bar{\alpha}_p \Delta T)| \le L(1 - x_{ep}), \qquad p = 1, 2; \ \forall e, \tag{30c}$$

$$|s_{et} - \bar{k}_{etp} \boldsymbol{b}_{et}^\top \boldsymbol{u}| \le L(1 - x_{ep}), \qquad\qquad t = 2, 3; \ p = 1, 2; \ \forall e, \tag{30d}$$

$$\frac{|s_{e1}|}{\bar{A}} + \frac{l_e |s_{e2}|}{2\bar{Z}} + \frac{|s_{e3}|}{\bar{Z}} \le \sum_{p=1}^{2} \bar{\sigma}_p^{\mathrm{u}} x_{ep}, \qquad\qquad \forall e, \tag{30e}$$

$$\sum_{e \in \mathcal{E}} \sum_{t=1}^{3} \tilde{s}_{et} \boldsymbol{b}_{et} = \tilde{\boldsymbol{f}}, \tag{30f}$$

$$|\tilde{s}_{et} - \bar{k}_{etp} \boldsymbol{b}_{et}^\top \tilde{\boldsymbol{u}}| \le L(1 - x_{ep}), \qquad\qquad t = 1, 2, 3; \ p = 1, 2; \ \forall e, \tag{30g}$$

$$\tilde{\boldsymbol{f}}^\top \tilde{\boldsymbol{u}} \le c^{\mathrm{u}}, \tag{30h}$$

$$\frac{|\tilde{s}_{e1}|}{\bar{A}} + \frac{l_e|\tilde{s}_{e2}|}{2\bar{Z}} + \frac{|\tilde{s}_{e3}|}{\bar{Z}} \leq \sum_{p=1}^{2} \bar{\sigma}_p^{\mathrm{u}} x_{ep}, \qquad \forall e, \tag{30i}$$

$$x_{e1} + x_{e2} + x_{e'1} + x_{e'2} \leq 1, \qquad \forall (e, e') \in \mathcal{E}_{\mathrm{cross}}, \tag{30j}$$

$$x_{e1} + x_{e2} \leq 1, \qquad \forall e, \tag{30k}$$

$$x_{e1}, x_{e2} \in \{0, 1\}, \qquad \forall e. \tag{30l}$$

Here, continuous variables are $\boldsymbol{u} \in \mathbb{R}^d, \tilde{\boldsymbol{u}} \in \mathbb{R}^d, s_{et} \in \mathbb{R}$, and $\tilde{s}_{et} \in \mathbb{R}$ ($\forall e \in \mathcal{E}$; $t = 1, 2, 3$), while 0-1 variables are x_{e1} and x_{e2} ($\forall e \in \mathcal{E}$). All the constraints other than the integrality constraints, (30l), are linear constraints. Thus, problem (30) is an MILP problem, and hence it can be solved globally with, e.g., a branch-and-cut method. Several software packages, e.g., CPLEX (IBM ILOG 2013), Gurobi Optimizer (Gurobi 2013), and SCIP (Achterberg 2009), are available for this purpose.

Remark 5 Constraints (30c), (30d), (30e), (30g), and (30i) involve absolute values. These constraints can be rewritten as some linear inequalities. For instance, constraint (30c) is reduced to

$$-L(1 - x_{ep}) \leq s_{e1} - \bar{k}_{e1p}(\boldsymbol{b}_{e1}^{\top}\boldsymbol{u} - l_e\bar{\alpha}_p\Delta T) \leq L(1 - x_{ep}), \quad p = 1, 2; \ \forall e.$$

The other constraints can be dealt with similarly.

Remark 6 In Remark 4, the constraint on symmetry in configuration of the base cell was formulated as (13). This constraint can also be rewritten in terms of 0-1 variables, x_{e1} and x_{e2} ($e \in \mathcal{E}$). Recall that $(e, e') \in \mathcal{E}_{\mathrm{sym}}$ means that member e and member e' are located at symmetric positions. Then the symmetry constraint, (13), is equivalently rewritten as

$$(x_{e1}, x_{e2}) = (x_{e'1}, x_{e'2}), \quad \forall (e, e') \in \mathcal{E}_{\mathrm{sym}}.$$

In practice, this condition is added to problem (30) as linear equality constraints.

Remark 7 The approach developed above can be extended to a case in which more than two constituent materials are available to design a structure. For instance, suppose that three materials, i.e., $\mathcal{M}_1$, $\mathcal{M}_2$, and $\mathcal{M}_3$, are available. Contrary to (24), in this case we use three 0–1 variables to express selection of material for member e as

$$\begin{aligned}
(x_{e1}, x_{e2}, x_{e3}) = (1, 0, 0) &\quad \Leftrightarrow \quad e \in \mathcal{M}_1, \\
(x_{e1}, x_{e2}, x_{e3}) = (0, 1, 0) &\quad \Leftrightarrow \quad e \in \mathcal{M}_2, \\
(x_{e1}, x_{e2}, x_{e3}) = (0, 0, 1) &\quad \Leftrightarrow \quad e \in \mathcal{M}_3, \\
(x_{e1}, x_{e2}, x_{e3}) = (0, 0, 0) &\quad \Leftrightarrow \quad e \in \mathcal{N}.
\end{aligned}$$

Constraint (25) is then replaced with

$$x_{e1} + x_{e2} + x_{e3} \leq 1.$$

The other constraints can also be rewritten by using x_{e1}, x_{e2}, and x_{e3} ($\forall e \in \mathcal{E}$) in a straightforward manner.

4 Separation of material distribution domains

A base cell consists of two materials. Distributions of the materials at the optimal solution can possibly become complicated. Then the base cell becomes assemblage of many small pieces, each of which consists of a single material; see Fig. 9d in Sect. 5.1 for a typical example. Such complex material distributions in a base cell may cause difficulty in the manufacture of the periodic structure. This motivates us in this section to develop a formulation of the design problem that can avoid mixture of material distributions. Section 4.1 introduces binary variables used for representing the material domains on a given ground structure. Section 4.2 shows that the design optimization problem with the separation constraint on material distributions can be recast as an MILP problem.

4.1 Notion of material domains

The optimal solution of the problem formulated in Sect. 3 may possibly have complicated material distributions in a base cell, which can be a source of difficulty in the actual fabrication process.[4] In the following, for an obtained base cell, we call the set of members consisting of a single material a *material domain*. We say that two material domains are *separated* if there exists a (closed) curve that separates two domains.

Steeves et al. (2007) used base cells with separated material domains to create planar periodic lattices exhibiting negative thermal expansion properties; subsequently, these lattices were studied further in Steeves and Evans (2011) and Steeves et al. (2009). In these base cells, the material with low thermal expansion is placed outside of the material with high thermal expansion. Hence, when temperature is elevated, compression forces will act on interfaces between two different materials. Due to these compression forces, bonding between two materials will be strengthened automatically. Thus, placing the material with low thermal expansion outside of the material with high thermal expansion might have a practical advantage. In the following, we suppose $\bar{\alpha}_1 > \bar{\alpha}_2$ without loss of generality and attempt to place $\mathcal{M}_2$ outside of $\mathcal{M}_1$. Note that we do not consider explicit constraints that prohibit tension forces at interfaces between two different materials.

---

[4] By using a modern sophisticated processing technique, we can probably fabricate periodic structures with complicated configurations. For instance, Chen et al. (2001) used a direct metal deposition, which melts powdered metals by laser, to fabricate a periodic structure with negative thermal expansion, which was found by three-phase topology optimization. Also, Qi and Halloran (2004) fabricated the structure in Chen et al. (2001) with microfabrication by co-extrusion, which is a powder based thermoplastic processing technique. Therefore, with such a processing technique, it is probably possible to fabricate the optimal solutions obtained by using the formulation in Sect. 3. In Sect. 4 we attempt to find a design which can be fabricated even with a more naive technique.

Therefore, at the optimal solution it is not guaranteed that forces acting at those interfaces are compressive.

To separate distributions of the two materials on a ground structure, we introduce the notion of material domains as follows. Recall that $\mathcal{E}$ is the set of members of the ground structure. Consider partition $\mathcal{E} = \mathcal{D}_1 \cup \mathcal{D}_2$ of $\mathcal{E}$, where $\mathcal{D}_1$ $\mathcal{D}_2$ are the sets of members that can be constituted by material 1 and material 2, respectively. Namely, $\mathcal{M}_1$ and $\mathcal{M}_2$ should satisfy

$$\mathcal{M}_1 \subseteq \mathcal{D}_1, \quad \mathcal{M}_2 \subseteq \mathcal{D}_2.$$

For node $i \in \mathcal{V}$, let $z_i \in \{0,1\}$ be a binary variable. We represent $\mathcal{D}_1$ and $\mathcal{D}_2$ by using z_i $(\forall i \in \mathcal{V})$ as

$$z_i + z_j \leq 1 \quad \Leftrightarrow \quad e = (i,j) \in \mathcal{D}_1, \tag{31a}$$

$$z_i + z_j = 2 \quad \Leftrightarrow \quad e = (i,j) \in \mathcal{D}_2; \tag{31b}$$

see Fig. 4 for an example. To place $\mathcal{M}_2$ outside of $\mathcal{M}_1$, we introduce the constraints that nodes near the center of the base cell satisfy $z_i = 0$ and nodes exterior of the base cell satisfy $z_i = 1$. Roughly speaking, if node i is farther than node j from the origin, O, in Fig. 4, then we impose the constraint

$$z_i \geq z_j; \tag{32}$$

see, for details, (39), (40), and (41) in section 4.2.

Besides z_i $(\forall i \in \mathcal{V})$, we use variable $x_e \in \{0,1\}$ which serves as an indicator of existence of member $e \in \mathcal{E}$. Namely, existence of member e is represented as

$$x_e = 1 \quad \Leftrightarrow \quad e \in \mathcal{M}_1 \cup \mathcal{M}_2, \tag{33a}$$

$$x_e = 0 \quad \Leftrightarrow \quad e \in \mathcal{N}. \tag{33b}$$

It follows from (31) and (33) that selection of the material for member e is expressed as

$$x_e = 1, \; z_i + z_j \leq 1 \quad \Leftrightarrow \quad e \in \mathcal{M}_1, \tag{34a}$$

$$x_e = 1, \; z_i + z_j = 2 \quad \Leftrightarrow \quad e \in \mathcal{M}_2, \tag{34b}$$

$$x_e = 0, \; z_i + z_j \leq 2 \quad \Leftrightarrow \quad e \in \mathcal{N}. \tag{34c}$$

In the optimization process we shall determine x_e $(\forall e \in \mathcal{E})$ and z_i $(\forall i \in \mathcal{V})$.

4.2 MILP formulation with domain separation constraint

This section demonstrates that, under the setting introduced in Sect. 4.1, the design optimization problem can be formulated as an MILP problem. To see this, we show that the constraints in Sect. 3.2, which have been formulated with variables $(x_{e1}, x_{e2}) \in \{0,1\}^2$ $(\forall e \in \mathcal{E})$, can now be rewritten with $x_e \in \{0,1\}$ $(\forall e \in \mathcal{E})$ and

Fig. 4 An example of values of z_i ($\forall i \in \mathcal{V}$) and the corresponding material domains, $\mathcal{D}_1$ and $\mathcal{D}_2$
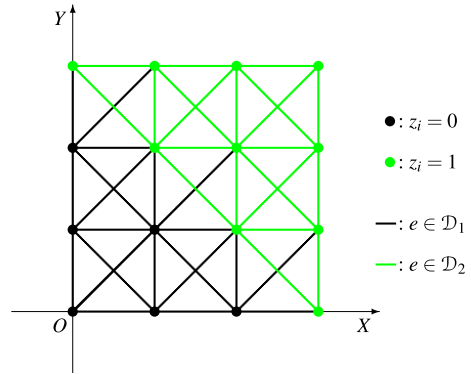
$z_i \in \{0, 1\}$ ($\forall i \in \mathcal{V}$). The equilibrium equations together with the stress constraints, the compliance constraint, the constraint prohibiting intersection of members, and the constraint on symmetry in the configuration are considered. Also, we handle the constraint separating the material domains, $\mathcal{D}_1$ and $\mathcal{D}_2$. All these constraints shall be formulated as linear constraints in terms of x_e's, z_i's, and some continuous variables.

We begin by rewriting (18), i.e., the equilibrium equation at the high temperature, with binary variables x_e and z_i. Since (18a) is independent of material selection, attention is focused on (18b) and (18c). Referring to (34), we can rewrite (18b) for each $e = (i, j) \in \mathcal{E}$ as

$$|s_{e1} - \bar{k}_{e11}(\boldsymbol{b}_{e1}^{\top}\boldsymbol{u} - l_e\bar{\alpha}_1\Delta T)| \leq L(1 - x_e + z_i), \tag{35a}$$

$$|s_{e1} - \bar{k}_{e11}(\boldsymbol{b}_{e1}^{\top}\boldsymbol{u} - l_e\bar{\alpha}_1\Delta T)| \leq L(1 - x_e + z_j), \tag{35b}$$

$$|s_{e1} - \bar{k}_{e12}(\boldsymbol{b}_{e1}^{\top}\boldsymbol{u} - l_e\bar{\alpha}_2\Delta T)| \leq L(3 - x_e - z_i - z_j), \tag{35c}$$

$$|s_{e1}| \leq Lx_e, \tag{35d}$$

where $L \gg 0$ is a sufficiently large constant. In the same manner, (18c) can be reduced to linear inequality constraints by using x_e, z_i, and z_j.

We next consider the stress constraints in (21), where σ_e^{u} is defined by (6). Referring to (34), we see that (21) with (6) can be rewritten by using x_e and z_i as

$$\frac{|s_{e1}|}{\bar{A}} + \frac{l_e|s_{e2}|}{2\bar{Z}} + \frac{|s_{e3}|}{\bar{Z}} \leq \bar{\sigma}_1^{\mathrm{u}}(2 - z_i - z_j) + \bar{\sigma}_2^{\mathrm{u}}z_i, \tag{36a}$$

$$\frac{|s_{e1}|}{\bar{A}} + \frac{l_e|s_{e2}|}{2\bar{Z}} + \frac{|s_{e3}|}{\bar{Z}} \leq \bar{\sigma}_1^{\mathrm{u}}(2 - z_i - z_j) + \bar{\sigma}_2^{\mathrm{u}}z_j, \tag{36b}$$

$$\frac{|s_{e1}|}{\bar{A}} + \frac{l_e|s_{e2}|}{2\bar{Z}} + \frac{|s_{e3}|}{\bar{Z}} \leq \bar{\sigma}_1^{\mathrm{u}}(1 + z_i + z_j) + \bar{\sigma}_2^{\mathrm{u}}(z_i + z_j). \tag{36c}$$

The equilibrium equations at the ordinary temperature are given by (20). Here, (20a) is a system of linear equality constraints. On the other hand, (20b) can be

rewritten as linear inequality constraints by using x_e and z_i in the same manner as (35). Also, the stress constraints, (22), can be reformulated in the same manner as (36).

The constraint prohibiting existence of mutually crossing members is given by (9g). By using (33), this constraint can be rewritten in terms of x_e's as

$$x_e + x_{e'} \leq 1, \quad \forall(e, e') \in \mathcal{E}_{\text{cross}}. \tag{37}$$

The constraint on symmetry of the base cell is formulated as follows. Unlike Remark 6, we now have to use variables x_e and z_i to write this constraint. Recall that $(e, e') \in \mathcal{E}_{\text{sym}}$ means that member e and member e' are located at symmetric positions. Similarly, we write $(i, j) \in \mathcal{V}_{\text{sym}}$ if node i is swapped with node j by the reflection depicted in Fig. 2(b). Then the symmetry constraint is given by

$$x_e = x_{e'}, \quad \forall(e, e') \in \mathcal{E}_{\text{sym}}, \tag{38a}$$

$$z_i = z_j, \quad \forall(i, j) \in \mathcal{V}_{\text{sym}}. \tag{38b}$$

Finally we consider the constraint for separating material domains, $\mathcal{D}_1$ and $\mathcal{D}_2$. An essential idea for this constraint has been sketched in Sect. 4.1; see (32). Explicit forms of this constraint depend on the shape of a ground structure. In this paper we restrict ourselves to ground structures with grid shapes such as the one in Fig. 4. Due to symmetry, we consider only the upper triangular portion. First, let $\mathcal{V}_{\text{upper}} \subset \mathcal{V}$ denote the set of nodes that are located above the diagonal line; see Fig. 5(a). For $i \in \mathcal{V}_{\text{upper}}$, the node located just below node i is called node The X-coordinates of node i and node $r_1(i)$ are the same. Hence, node i is farther than node $r_1(i)$ from the origin, O, of the coordinate system illustrated in Fig. 5. Recall that member $e = (i, j) \in \mathcal{E}$ can satisfy $(i, j) \in \mathcal{M}_2$ only if $z_i = z_j = 1$; see (31). Since we attempt to
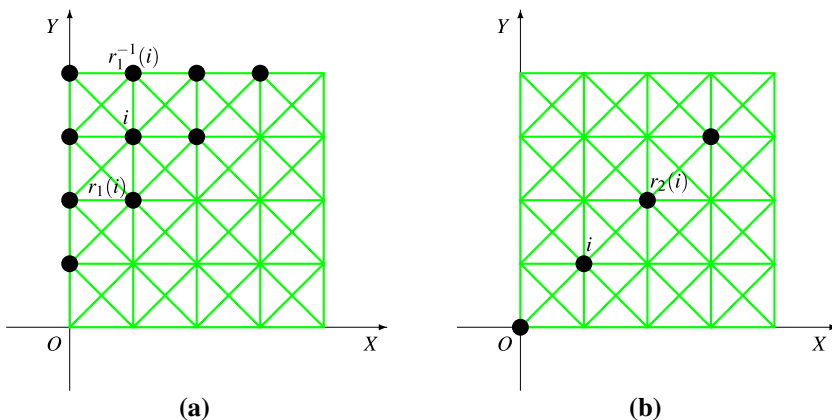

(a)   **(b)**

Fig. 5 Notation for the domain separation constraints. **a** The set of nodes depicted by *filled circles* is $\mathcal{V}_{\text{upper}}$; and **b** the set of nodes depicted by *filled circles* is $\mathcal{V}_{\text{diag}}$

place $\mathcal{M}_2$ outside of $\mathcal{M}_1$, we require $z_{r_1}(i) = 0$ if the outside node, $i \in \mathcal{V}_{\text{upper}}$, satisfies $z_i = 0$. For this reason we consider the following constraint:

$$z_i \geq z_{r_1(i)}, \quad \forall i \in \mathcal{V}_{\text{upper}}. \tag{39}$$

Second, consider the nodes on the diagonal of the base cell. We denote by $\mathcal{V}_{\text{diag}} \subset \mathcal{V}$ the set of these nodes as shown in Fig. 5(b). Note that we exclude the top rightmost node from $\mathcal{V}_{\text{diag}}$ for notational convenience. For $i \in \mathcal{V}_{\text{diag}}$, the diagonal node just outside of node i is called node $r_2(i)$. Node $r_2(i)$ is farther than node i from the origin, O. Hence, if $z_{r_2(i)x} = 0$, then the inside node, i, should satisfy $z_i = 0$. This motivates us to consider the following constraint:

$$z_{r_2(i)} \geq z_i, \quad \forall i \in \mathcal{V}_{\text{diag}}. \tag{40}$$

For $i \in \mathcal{V}_{\text{diag}}$, consider nodes $r_1^{-1}(i)$ and $r_2(i)$, where $r_1^{-1}(i)$ is defined by $r_1(r_1^{-1}(i)) = i$. As listed in Fig. 6, there exist five cases of $(z_i, z_{r_1^{-1}(i)}, z_{r_2(i)})$ satisfying (39) and (40). Among these five patterns, only the rightmost one is not acceptable, because a member of $\mathcal{M}_2$ is surrounded by members of $\mathcal{M}_1$. It is observed from the bottom row of Fig. 6 that this unacceptable pattern can be excluded by adding the following constraint:

$$z_{r_1^{-1}(i)} \leq z_{r_2(i)} + z_i, \quad \forall i \in \mathcal{V}_{\text{diag}}. \tag{41}$$

Thus all the constraints are written as linear constraints in terms of $\boldsymbol{u} \in \mathbb{R}^d, \tilde{\boldsymbol{u}} \in \mathbb{R}^d, s_{et} \in \mathbb{R}, \tilde{s}_{et} \in \mathbb{R}, x_e \in \{0, 1\}$, and $s_i \in \{0, 1\}$ ($\forall e \in \mathcal{E}$; $\forall i \in \mathcal{V}$; $t = 1, 2, 3$). Therefore, the optimization problem considered in this section can be recast as an MILP problem.

We elaborate the full description of this MILP formulation with comparing with MILP problem (30) in Sect. 3.2, i.e., the one without the separation constraint. First, the objective function is same as the one of problem (30). Namely, we minimize the displacement of the interface node, u_1.

Second, the constraints are given as follows.

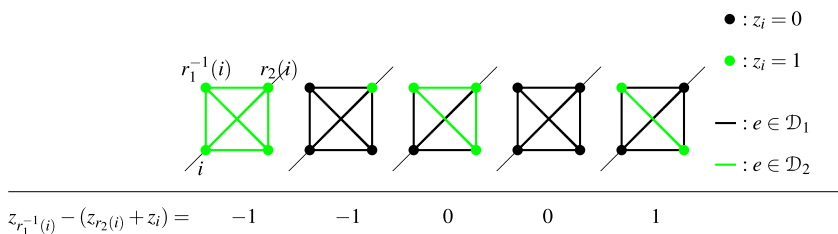– Constraints (30b), (30f), and (30h) are retained without change, i.e.,

Fig. 6 Enumeration of $(z_i, z_{r_1^{-1}(i)}, z_{r_2(i)})$ satisfying (39) and (40) for $i \in \mathcal{V}_{\text{diag}}$ and the corresponding material distributions. The values of $z_{r_1^{-1}(i)} - (z_{r_2(i)} + z_i)$ are listed in the bottom row

$$\sum_{e \in \mathcal{E}} \sum_{t=1}^{3} s_{et} \boldsymbol{b}_{et} = \boldsymbol{f}, \tag{42}$$

$$\sum_{e \in \mathcal{E}} \sum_{t=1}^{3} \tilde{s}_{et} \boldsymbol{b}_{et} = \tilde{\boldsymbol{f}}, \tag{43}$$

$$\tilde{\boldsymbol{f}}^{\top} \tilde{\boldsymbol{u}} \le c^{\mathrm{u}}. \tag{44}$$

- Corresponding to constraints (30c) and (30d), relations between the generalized stresses and the displacements caused by the elevation of temperature are given as

$$|s_{e1} - \bar{k}_{e11}(\boldsymbol{b}_{e1}^{\top}\boldsymbol{u} - l_e \bar{\alpha}_1 \Delta T)| \le L(1 - x_e + z_i), \quad \forall e = (i,j),$$
$$|s_{e1} - \bar{k}_{e11}(\boldsymbol{b}_{e1}^{\top}\boldsymbol{u} - l_e \bar{\alpha}_1 \Delta T)| \le L(1 - x_e + z_j), \quad \forall e = (i,j),$$
$$|s_{e1} - \bar{k}_{e12}(\boldsymbol{b}_{e1}^{\top}\boldsymbol{u} - l_e \bar{\alpha}_2 \Delta T)| \le L(3 - x_e - z_i - z_j), \quad \forall e = (i,j),$$
$$|s_{e1}| \le L x_e, \quad \forall e$$

and

$$|s_{et} - \bar{k}_{et1} \boldsymbol{b}_{et1}^{\top}\boldsymbol{u}| \le L(1 - x_e + z_i), \quad t = 2,3; \ \forall e = (i,j),$$
$$|s_{et} - \bar{k}_{et1} \boldsymbol{b}_{et1}^{\top}\boldsymbol{u}| \le L(1 - x_e + z_j), \quad t = 2,3; \ \forall e = (i,j),$$
$$|s_{et} - \bar{k}_{et2} \boldsymbol{b}_{et1}^{\top}\boldsymbol{u}| \le L(3 - x_e - z_i - z_j), \quad t = 2,3; \ \forall e = (i,j),$$
$$|s_{et}| \le L x_e, \quad t = 2,3; \ \forall e.$$

- Instead of (30e), the stress constraints at the elevated temperature are written as

$$\frac{|s_{e1}|}{\bar{A}} + \frac{l_e|s_{e2}|}{2\bar{Z}} + \frac{|s_{e3}|}{\bar{Z}} \le \bar{\sigma}_1^{\mathrm{u}}(2 - z_i - z_j) + \bar{\sigma}_2^{\mathrm{u}} z_i, \quad \forall e = (i,j),$$
$$\frac{|s_{e1}|}{\bar{A}} + \frac{l_e|s_{e2}|}{2\bar{Z}} + \frac{|s_{e3}|}{\bar{Z}} \le \bar{\sigma}_1^{\mathrm{u}}(2 - z_i - z_j) + \bar{\sigma}_2^{\mathrm{u}} z_j, \quad \forall e = (i,j),$$
$$\frac{|s_{e1}|}{\bar{A}} + \frac{l_e|s_{e2}|}{2\bar{Z}} + \frac{|s_{e3}|}{\bar{Z}} \le \bar{\sigma}_1^{\mathrm{u}}(1 + z_i + z_j) + \bar{\sigma}_2^{\mathrm{u}}(z_i + z_j), \quad \forall e = (i,j).$$

- Corresponding to constraint (30g), relations between the generalized stresses and the displacements caused by the fictitious external load are given as

$$|\tilde{s}_{et} - \bar{k}_{et1} \boldsymbol{b}_{et}^{\top}\tilde{\boldsymbol{u}}| \le L(1 - x_e + z_i), \quad t = 1,2,3; \ \forall e = (i,j),$$
$$|\tilde{s}_{et} - \bar{k}_{et1} \boldsymbol{b}_{et}^{\top}\tilde{\boldsymbol{u}}| \le L(1 - x_e + z_j), \quad t = 1,2,3; \ \forall e = (i,j),$$
$$|\tilde{s}_{et} - \bar{k}_{et2} \boldsymbol{b}_{et}^{\top}\tilde{\boldsymbol{u}}| \le L(3 - x_e - z_i - z_j), \quad t = 1,2,3; \ \forall e = (i,j),$$
$$|\tilde{s}_{et}| \le L x_e, \quad t = 1,2,3; \ \forall e.$$

- Instead of constraint (30i), the stress constraints at the ordinary temperature are given as

$$\frac{|\tilde{s}_{e1}|}{\bar{A}} + \frac{l_e|\tilde{s}_{e2}|}{2\bar{Z}} + \frac{|\tilde{s}_{e3}|}{\bar{Z}} \leq \bar{\sigma}_1^{u}(2 - z_i - z_j) + \bar{\sigma}_2^{u}z_i, \qquad \forall e = (i,j),$$

$$\frac{|\tilde{s}_{e1}|}{\bar{A}} + \frac{l_e|\tilde{s}_{e2}|}{2\bar{Z}} + \frac{|\tilde{s}_{e3}|}{\bar{Z}} \leq \bar{\sigma}_1^{u}(2 - z_i - z_j) + \bar{\sigma}_2^{u}z_j, \qquad \forall e = (i,j),$$

$$\frac{|\tilde{s}_{e1}|}{\bar{A}} + \frac{l_e|\tilde{s}_{e2}|}{2\bar{Z}} + \frac{|\tilde{s}_{e3}|}{\bar{Z}} \leq \bar{\sigma}_1^{u}(1 + z_i + z_j) + \bar{\sigma}_2^{u}(z_i + z_j), \quad \forall e = (i,j).$$

- Instead of constraint (30j), the constraint prohibiting intersection of members is given as

$$x_e + x_{e'} \leq 1, \quad \forall(e, e') \in \mathcal{E}_{\text{cross}}.$$

- Concerning symmetry of the base cell, we have the following constraints:

$$x_e = x_{e'}, \quad \forall(e, e') \in \mathcal{E}_{\text{sym}},$$
$$z_i = z_j, \quad \forall(i, j) \in \mathcal{V}_{\text{sym}}.$$

- Concerning separation of material distributions, we have the following constraints:

$$z_{r_1(i)} \leq z_i, \quad \forall i \in \mathcal{V}_{\text{upper}},$$
$$z_i \leq z_{r_2(i)}, \quad \forall i \in \mathcal{V}_{\text{diag}},$$
$$z_{r_1^{-1}(i)} \leq z_i + z_{r_2(i)}, \quad \forall i \in \mathcal{V}_{\text{diag}}.$$

- Finally, binary constraints are

$$x_e \in \{0, 1\}, \quad \forall e \in \mathcal{E},$$
$$z_i \in \{0, 1\}, \quad \forall i \in \mathcal{V}.$$

Thus the optimization problem is an MILP problem, where $\boldsymbol{u} \in \mathbb{R}^d, \tilde{\boldsymbol{u}} \in \mathbb{R}^d, s_{et} \in \mathbb{R}, \tilde{s}_{et} \in \mathbb{R}, x_e \in \{0, 1\}$, and $s_i \in \{0, 1\}$ ($\forall e \in \mathcal{E}; \ \forall i \in \mathcal{V}; \ t = 1, 2, 3$) are variables to be optimized.

5 Numerical experiments

In this section we perform numerical experiments by solving the proposed MILP problems. Section 5.1 collects design examples of the formulation presented in Sect. 3 (called formulation (I)), while Sect. 5.2 collects the ones of the formulation developed in Sect. 4 (called formulation (II)). Section 5.3 examines a simple heuristic strategy, using techniques already implemented in the MILP solver, for larger instances. Computation was carried out on 2.66 GHz 6-Core Intel Xeon Westmere processors with 64 GB RAM. MILP problems were solved by using CPLEX ver. 12.2 (IBM ILOG 2013). As for parameters of CPLEX, the integrality

tolerance and feasibility tolerance were set to $= 10^{-8}$. The other parameters of CPLEX were set to the default values.

Each existing member has a rectangular cross-section with width $\bar{w} = 1\,\text{mm}$ and thickness $\bar{t} = 1\,\text{mm}$. The cross-sectional area, the elastic section modulus, and the moment of inertia are given by

$$\bar{A} = \bar{t}\bar{w} = 1\,\text{mm}^2, \quad \bar{Z} = \frac{1}{6}\bar{t}\bar{w}^2 = \frac{1}{6}\,\text{mm}^3, \quad \bar{I} = \frac{1}{12}\bar{t}\bar{w}^3 = \frac{1}{12}\,\text{mm}^4.$$

The shear correction factor of Timoshenko elements is $\kappa = 5/6$. The constant L in problem (30) is given as follows. We actually use different values for $e \in \mathcal{E}, t = 1, 2, 3$, and $p = 1, 2$. Namely, the constants on the right-hand side of (30c) are specified as $L_{e1p} = \bar{k}_{e1p}l_e/l_{\text{cell}}$, where l_{cell} is the side length of a unit cell. The constants on the right-hand side of (30d) are

$$L_{e2p} = \frac{1}{l_{\text{cell}}}\left(\frac{l_{\text{cell}}^2}{12\bar{E}_p\bar{I}} + \frac{1}{\kappa\bar{G}_p\bar{A}}\right)^{-1}, \quad L_{e3p} = \bar{k}_{e3p}\frac{l_e}{l_{\text{cell}}}.$$

The constants L in (30g) are specified in a similar manner. These values were determined from preliminary numerical experiments, although there might remain room for tightening these values. It seems to be difficult to predict the smallest allowable value of L in advance.

The material parameters of two constituent materials, approximating an aluminium alloy (7075-T6) and a titanium alloy (Ti-6Al-4V), are listed in Table 2. The temperature change is $\Delta T = 200\,\text{K}$. The side length of a unit cell is $l_{\text{cell}} = 24\,\text{mm}$. Concerning the compliance constraint in (30h), the upper bound for the compliance is $c^u = 10^{-2}\,\text{J}\,(= 10^{-2}\,\text{N} \cdot \text{m})$ and a force of $1\,\text{N}$ is applied as fictitious external load, $\tilde{f}$. As explained in Sect. 2.2, this compliance constraint is used to avoid meaningless solutions by ensuring that there exists a connected path between interface nodes. Certainly, c^u can be set to a smaller value if more global stiffness, in terms of the compliance against the assumed external load, is required.

5.1 Formulation (I)

This section presents the results obtained by solving problem (30) in Sect. 3.2. Hence, the separation constraint on material distributions is not considered. As for connection pattern of base cells, the two cases shown in Fig. 1 are considered. We consider the two ground structures shown in Fig. 7. The frame structure in Fig. 7a

Table 2 Material properties of the constituent materials used in the numerical examples

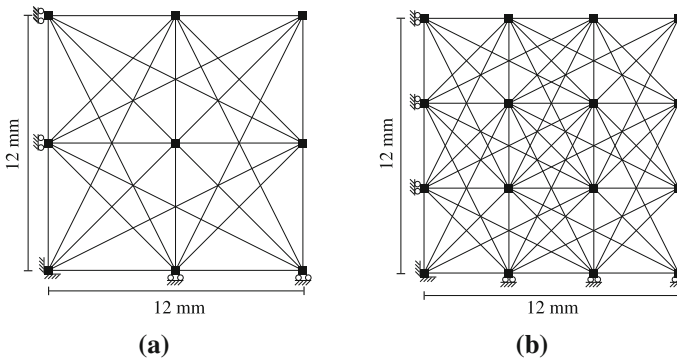|	Material 1 ($\mathcal{M}_1$)	Material 2 ($\mathcal{M}_2$)
Young's modulus	$\bar{E}_1 = 70\,\text{GPa}$	$\bar{E}_2 = 110\,\text{GPa}$
Shear modulus	$\bar{G}_1 = 25\,\text{GPa}$	$\bar{G}_2 = 45\,\text{GPa}$
Thermal expansion coefficient	$\bar{\alpha}_1 = 25 \times 10^{-6}\,\text{K}^{-1}$	$\bar{\alpha}_2 = 10 \times 10^{-6}\,\text{K}^{-1}$
Upper bound for stress	$\bar{\sigma}_1^u = 340\,\text{MPa}$	$\bar{\sigma}_2^u = 860\,\text{MPa}$

Fig. 7 The ground structures for the experiments with formulation (I). **a** The frame structure with $|\mathcal{V}| = 3 \times 3$ nodes; and **b** the frame structure with $|\mathcal{V}| = 4 \times 4$ nodes

consists of $|\mathcal{V}| = 3 \times 3 = 9$ nodes and $|\mathcal{E}| = 28$ members, while the one in Fig. 7b consists of $|\mathcal{V}| = 4 \times 4 = 16$ nodes and $|\mathcal{E}| = 66$ members.

5.1.1 Connection pattern (A) with formulation (I)

We begin with the results for connection pattern (A). The optimal solutions obtained for the two ground structures are shown in Fig. 8a and c. In these figures, black lines and gray lines show members that consist of material 1 ($\mathcal{M}_1$) and material 2 ($\mathcal{M}_2$), respectively. The computational results are listed in Table 3. Here, "time" shows the computational time spent by CPLEX (IBM ILOG 2013), "# of nodes" reports the number of enumeration nodes explored by CPLEX, "# of cuts" is the number of cuts added by CPLEX, and the optimal value means the displacement of the interface node. Since the optimal values are negative in both cases, structures possessing thermal contraction properties are successfully obtained. CPLEX requires more than 66 h to solve the problem instance with the larger ground structure in Fig. 7b.

Figure 8b and d show the optimized base cells. Deformations due to the thermal increase, $\Delta T = 200\,\mathrm{K}$, are also depicted in these figures, where displacements are magnified $\times 20$. It is observed in Fig. 8b that $\mathcal{M}_1$, i.e., the material with the higher thermal expansion coefficient, forms a star-shaped octagon, i.e., an octagon with four reentrant corners. Also, in Fig. 8d we can find a reentrant polygon consisting of $\mathcal{M}_1$. Similar shapes can be found in structures with negative Poisson's ratio (Sigmund and Torquato 1997); see, e.g., Lakes (1987), Kureta and Kanno (2014), and Theocaris et al. (1997) for star-shaped structures with negative Poisson's ratio.

5.1.2 Connection pattern (B) with formulation (I)

We next consider connection pattern (B). The two ground structures in Fig. 7 are used. For connection pattern (B), we minimize the vertical displacement of the top-right node.
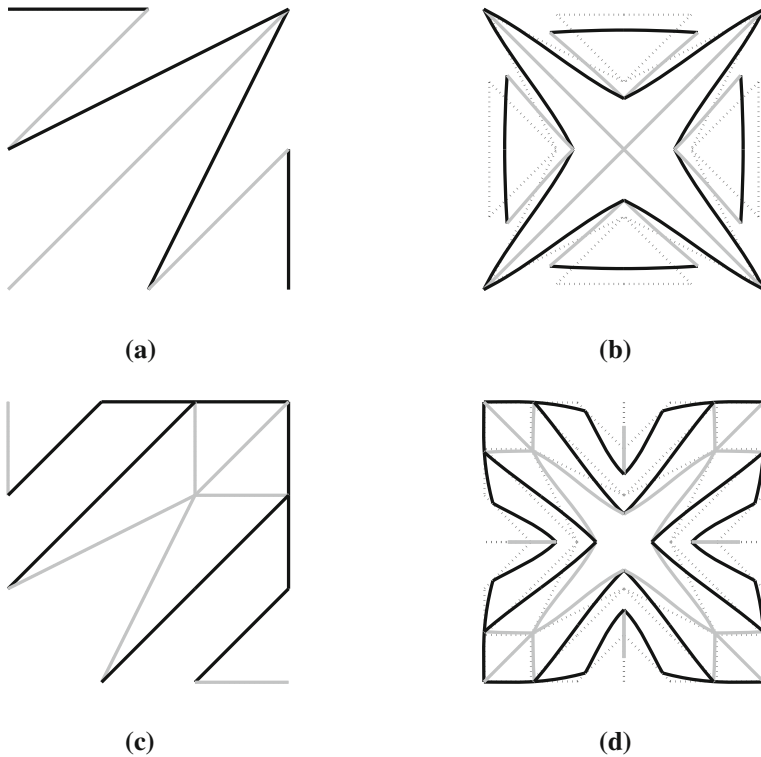
Fig. 8 The optimal solutions of formulation (I) with connection pattern (A). **a** The optimal topology obtained from the ground structure in Fig. 7a; and **b** its deformed configuration at the high temperature. **c**) The optimal topology obtained from the ground structure in Fig. 7b; and **d** its deformed configuration at the high temperature. *Black lines* show $\mathcal{M}_1$ (material 1) and gray lines show $\mathcal{M}_2$ (material 2). Displacements in (b) and (d) are magnified ×20

Table 3 Computational results of the experiments with formulation (I)

$|\mathcal{V}|$	Pattern	Time (s)	# of nodes	# of cuts	Optimal value (mm)
3×3	(A)	14.2	21,891	15	-6.8785×10^{-2}
4×4	(A)	237,712.7	101,573,597	95	-10.0626×10^{-2}
3×3	(B)	23.3	52,381	22	-0.8437×10^{-2}
4×4	(B)	490,286.8	474,076,549	94	-4.6005×10^{-2}

The optimal solutions are shown in Fig. 9a and c. The computational results are listed in Table 3. Figure 9b and d show the thermal deformations of the optimized base cells. Material 1 ($\mathcal{M}_1$) in Fig. 9b forms a dodecagon with four reentrant corners. In Fig. 9d, we can find a star-shaped octagon consists of material 1. In this base cell, distributions of the two materials are intricately mixed. In contrast, distributions in Fig. 9b are separated quite clearly. Indeed, in this solution, the four
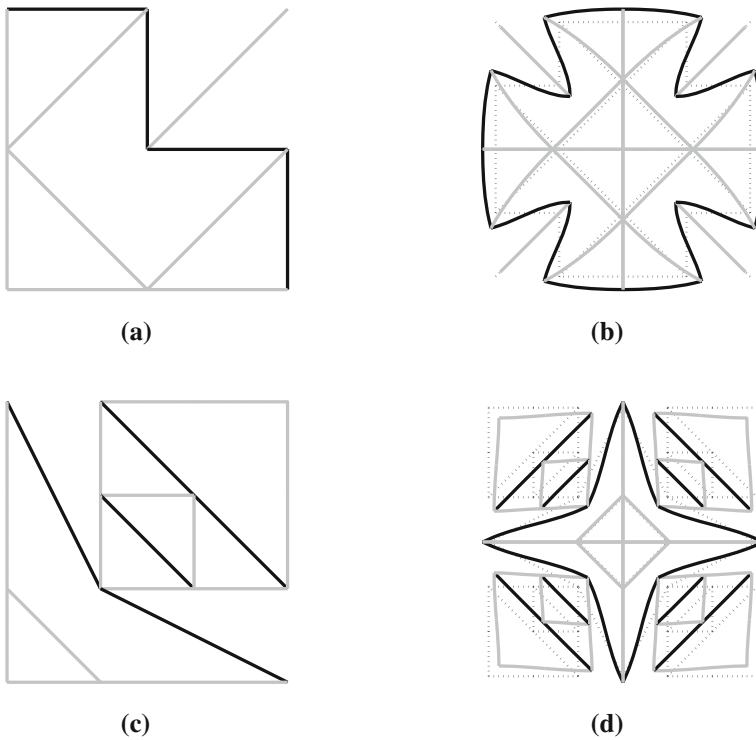
Fig. 9 The optimal solutions of formulation (I) with connection pattern (B). **a** The optimal topology obtained from the ground structure in Fig. 7a; and **b** its deformed configuration at the high temperature (displacements are magnified ×50). **c** The optimal topology obtained from the ground structure in Fig. 7b; and **d** its deformed configuration at the high temperature (displacements are magnified ×20). *Black lines* show $\mathcal{M}_1$(material 1) and *gray lines* show $\mathcal{M}_2$ (material 2)

exterior members consisting of material 2 are used for connection with adjacent cells can be replaced by material 1, although this makes the objective value worse a little. The negative thermal expansion property stems mainly from the reentrant dodecagon and its interior members.

The optimized base cells obtained in Sects. 5.1.1 and 5.1.2 have the following characteristics; see Figs. 8b, d and 9b, d. The material with high thermal expansion ($\mathcal{M}_1$) forms a polygon with some reentrant corners. A structure consisting of the material with low thermal expansion ($\mathcal{M}_2$) is placed inside of the polygon. When temperature is elevated, expansion of the polygon is partially blocked by the interior structure and, as a result, the reentrant corners of the polygon move towards interior of the base cell. This explains the negative thermal expansion properties of the obtained solutions. Also, from this observation we see that the interfaces between the two different materials, i.e., the interfaces of the reentrant polygon ($\mathcal{M}_1$) and its interior structure ($\mathcal{M}_2$), primarily undergo tension forces. In contrast, in Sect. 5.2 we explore base cells such that $\mathcal{M}_1$ is surrounded by $\mathcal{M}_2$ by using the formulation developed in Sect. 4. In such a solution we expect that the interfaces between the two different materials undergo compression forces.
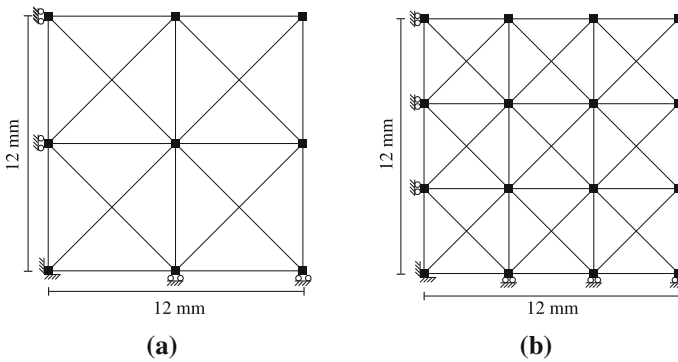
Fig. 10 The ground structures for the experiments with formulation (II). **a** The frame structure with $|\mathcal{V}| = 3 \times 3$ nodes; and **b** the frame structure with $|\mathcal{V}| = 4 \times 4$ nodes

5.2 Formulation (II)

This section performs the numerical experiments that incorporates the separation constraint on material distribution, which has been presented in Sect. 4. We consider the two ground structures shown in Fig. 10. The frame structure in Fig. 10a consists of $|\mathcal{V}| = 3 \times 3$ nodes and $|\mathcal{E}| = 20$ members, while the one in Fig. 10b consists of $|\mathcal{V}| = 4 \times 4$ nodes and $|\mathcal{E}| = 42$ members. As for connection pattern of base cells, the two cases shown in Fig. 1 are considered.

5.2.1 Connection pattern (A) with formulation (II)

We first consider connection pattern (A). The optimal solutions obtained for the two ground structures in Fig. 10 are shown in Fig. 11a and c. Figure 11b and d show the thermal deformations of the optimal base cells. It is observed in these figures that $\mathcal{M}_2$, i.e., the material with lower thermal expansion coefficient, is distributed on the outer side of $\mathcal{M}_1$, i.e., the one with the higher thermal expansion coefficient. Moreover, in Fig. 11d, $\mathcal{M}_1$ forms a hexadecagon with four reentrant corners.

The computational time and the optimal values are listed in Table 4. It is observed that in both cases the optimal solutions realize thermal contraction. CPLEX requires about 2.6 h to solve the larger instance.

5.2.2 Connection pattern (B) with formulation (II)

We next consider connection pattern (B). The obtained optimal solutions are shown in Fig. 12a and c. The thermal deformations of the optimal base cells are depicted in Fig. 12b and d. The computational costs and the optimal values are listed in Table 4. In these examples, both solutions do not exhibit negative thermal expansion.

Finally we discuss properties of the optimal solutions obtained in Sects. 5.2.1 and 5.2.2; see Figs. 11a, d and 12b, d. The low thermal expansion material ($\mathcal{M}_2$) is placed outside of the high thermal expansion material ($\mathcal{M}_1$), as expected. Particularly, it is observed in Fig. 12(d) that, when temperature is elevated, the

(a)   (b)

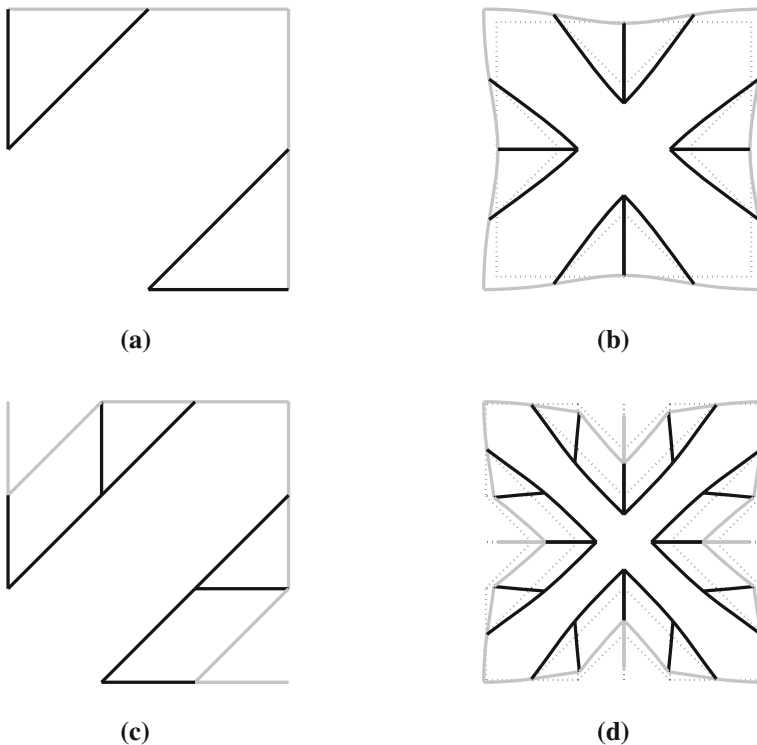(c)   (d)

Fig. 11 The optimal solutions of formulation (II) with connection pattern (A). **a** The optimal topology obtained from the ground structure in Fig. 10a; and **b** its deformed configuration at the high temperature (displacements are magnified ×50). **c** The optimal topology obtained from the ground structure in Fig. 10b; and **d** its deformed configuration at the high temperature (displacements are magnified ×20). *Black lines* show $\mathcal{M}_1$ (material 1) and *gray lines* show $\mathcal{M}_2$ (material 2)

Table 4 Computational results of the experiments with formulation (II)

$|\mathcal{V}|$	Pattern	Time (s)	# of nodes	# of cuts	Optimal value (mm)
3 × 3	(A)	7.0	7836	29	-0.2597×10^{-2}
4 × 4	(A)	9499.5	4,274,215	222	-5.1059×10^{-2}
3 × 3	(B)	5.8	7514	54	2.3919×10^{-2}
4 × 4	(B)	11,269.0	8,974,070	236	0.1864×10^{-2}

four interfaces between $\mathcal{M}_1$ and $\mathcal{M}_2$ undergo compression forces. Therefore, bonding between two materials is automatically strengthened by elevation of temperature. From a practical point of view, this might be an advantage over the solutions obtained in Sect. 5.1. However, the solution in Fig. 12d has a, very small but, nonnegative thermal expansion coefficient. Essential mechanism from which near zero thermal expansion stems is similar to the ones studied by Steeves et al. (2007). In the solutions shown in Figs. 11b, d and 12b, the interior structures
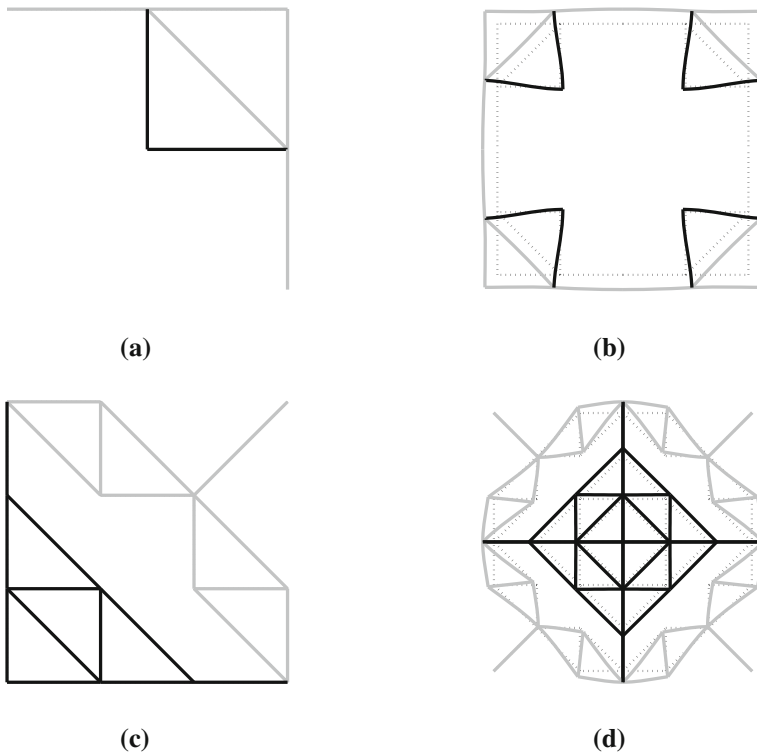
Fig. 12 The optimal solutions of formulation (II) with connection pattern (B). **a** The optimal topology obtained from the ground structure in Fig. 10a; and **b** its deformed configuration at the high temperature (displacements are magnified ×50). **c** The optimal topology obtained from the ground structure in Fig. 10b; and **d** its deformed configuration at the high temperature (displacements are magnified ×20). *Black lines* show $\mathcal{M}_1$ (material 1) and *gray lines* show $\mathcal{M}_2$ (material 2)

consisting of material 1 ($\mathcal{M}_1$) are disconnected. A unit cell with a negative thermal expansion property and a connected interior structure consisting of $\mathcal{M}_1$ is found in the experiment presented in Sect. 5.3.2.

5.3 A heuristic approach

It was observed in Sects. 5.1 and 5.2 that the MILP solver, CPLEX, requires large computational time to solve the problems of the grand structures with $|\mathcal{V}| = 4 \times 4 = 16$ nodes. In this section we attempt to obtain high quality, hopefully nearly optimal, solutions of larger instances by making use of the heuristics already implemented in the MILP solver. Sometimes it happens that the solver finds very good solutions quickly and spends a large amount of time proving the optimality of the incumbent solution or make minor improvements to it. In such a case, the best feasible solution found within a limited small amount of time can be adopted as a good solution, if we do not require proof of optimality. This simple strategy is tested as a heuristic to large instances. We use `timelimit` parameter to specify the

maximum time that CPLEX can spend trying to solve an instance and report the best feasible solution. The `emphasis mip` parameter of CPLEX is set to four (emphasize to find hidden feasible solutions). In Sect. 5.3.1 we solve the instances in Sects. 5.1 and 5.2 with the time limit to compare the results with the global optimal solutions obtained without time limit. Section 5.3.2 is devoted to larger instances that are difficult to be solved without time limit. The displacements in the following figures are magnified ×20.

5.3.1 Comparison to solutions with guaranteed optimality

The problem instances that have been solved in Sects. 5.1 and 5.2 are solved in this section with the time limit to compare the results with the global optimal solutions. The ground structures shown in Figs. 7b and 10b, respectively, are used for formulations (I) and (II). Both connection patterns (A) and (B) are considered for each formulation. As for time limit, we consider two cases, 300 and 1000 s.

The computational results are listed in Table 5. Here, "best obj." reports the objective value of the best feasible solution, and "gap" means the difference between "best obj." and the objective value of the best node remaining. In all the cases, the global optimal solutions are found within 1000 s. Moreover, for formulation (II) with connection pattern (A), CPLEX spent less than 300 s finding the global optimal solution. In contrast, in the other three cases the best solutions obtained within 300 s are not optimal. These solutions are shown in Fig. 13. The solution in Fig. 13b has an exterior part that forms a reentrant polygon consisting of the material with the higher thermal expansion coefficient. This part is same as that of the global optimal solution in Fig. 8d. The *star-shaped* octagon and its interior core of the solution in Fig. 13b are same as those the global optimal solution in Fig. 9d. However, the exterior part has four unstressed members and has room for improvement. The solution in Fig. 13c has the interior and exterior parts with sizes different from the global optimal solution in Fig. 12d, although it has analogous mechanism in essence for achieving a small thermal expansion coefficient.

Table 5 Computational results of the experiments in Sect. 5.3.1

| Ex.	$|\mathcal{V}|$	Pattern	# of nodes	# of cuts	Gap (mm)	Best obj. (mm)	Time (s)
(I)	4×4	(A)	47,253	11	44.8474×10^{-2}	-8.7499×10^{-2}	300.0
(I)	4×4	(B)	73,536	13	103.4748×10^{-2}	-3.8472×10^{-2}	300.0
(II)	4×4	(A)	50,904	60	46.8032×10^{-2}	-5.1059×10^{-2}	300.0
(II)	4×4	(B)	72,189	74	61.6548×10^{-2}	0.6752×10^{-2}	300.0
(I)	4×4	(A)	199,633	13	31.1607×10^{-2}	-10.0626×10^{-2}	1000.0
(I)	4×4	(B)	323,581	19	77.0312×10^{-2}	-4.6005×10^{-2}	1000.0
(II)	4×4	(A)	259,046	74	26.2411×10^{-2}	-5.1059×10^{-2}	1000.0
(II)	4×4	(B)	566,646	76	17.9724×10^{-2}	0.1864×10^{-2}	1000.0
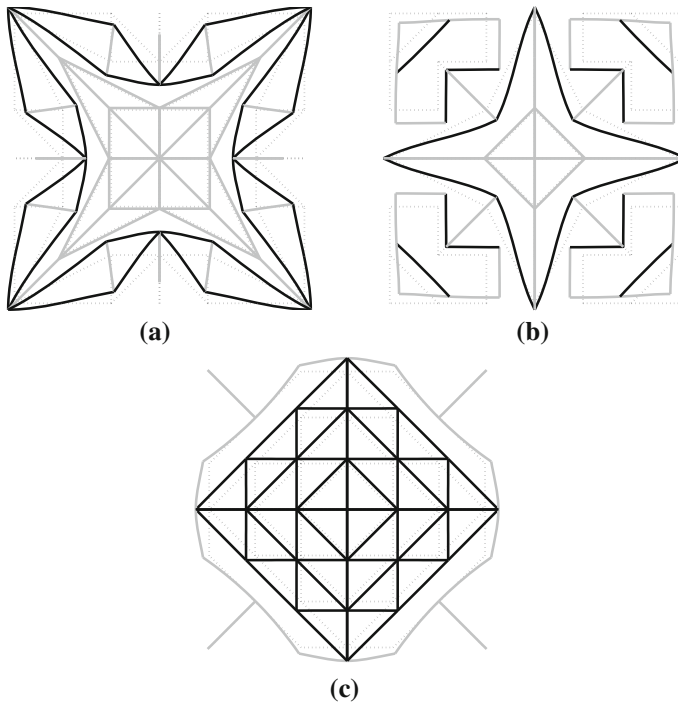
Fig. 13 The best feasible solutions obtained by running the MILP solver for 300 s. The solutions for **a** formulation (I) with $|\mathcal{V}| = 4 \times 4$ and pattern (A); **b** formulation (I) with $|\mathcal{V}| = 4 \times 4$ and pattern (B); and **c** formulation (II) with $|\mathcal{V}| = 4 \times 4$ and pattern (B)

5.3.2 Large-scale examples with the heuristic approach

In this section we apply the heuristic approach to some problem instances that are larger than the ones solved above, where the MILP solver is run with time limit 43,200 s $= 12$ h. Therefore, optimality of the solutions obtained in this section is not guaranteed.

We begin with formulation (I) with the ground structures shown in Fig. 14. The frame structure in Fig. 14a consists of $|\mathcal{V}| = 5 \times 5 = 25$ nodes and $|\mathcal{E}| = 120$ members, the one in Fig. 14b consists of $|\mathcal{V}| = 4 \times 4 = 16$ nodes and $|\mathcal{E}| = 86$ members, and the one in Fig. 14c consists of $|\mathcal{V}| = 5 \times 5 = 25$ nodes and $|\mathcal{E}| = 200$. The obtained solutions are collected in Figs. 15 and 16. The computational results are listed in Table 6.

The obtained solutions with connection pattern (A) are shown in Fig. 15a, b, and c. In view of Figs. 8b, 15b and c, we might figure out a common feature of the mechanisms from which the negative thermal expansion properties stem. That is, in Fig. 8b, the material with the higher thermal expansion coefficient forms a star-shaped octagon. The solutions in Fig. 15b and c have two nested star-shaped octagons, which may possibly suggest an optimal fractal structure at the limit of the
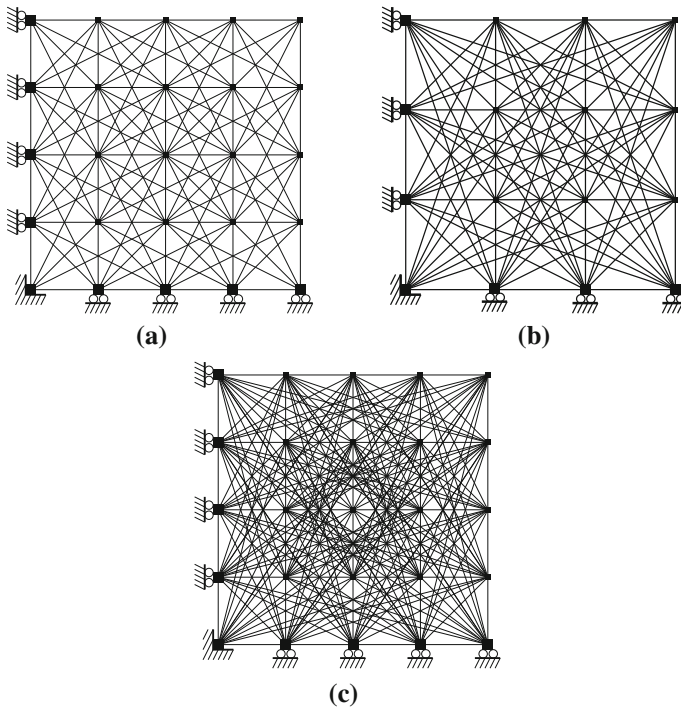
Fig. 14 The ground structures for the heuristic method with formulation (I). The frame structures with **a** $|\mathcal{E}| = 120$ members; **b** $|\mathcal{E}| = 86$ members; and **c** $|\mathcal{E}| = 200$ members

finer ground structure. The solutions in Fig. 15a, b and c have better objective values than the solution in Fig. 8d. Moreover, the objective value of the solution in Fig. 15b is better than that of Fig. 15a and the objective value of the solution in Fig. 15c is better than that of Fig. 15b; increase of the number of nodes and increase of the number of members improve the objective value. Concerning connection pattern (B), the objective value of the solution in Fig. 15d (for the $|\mathcal{V}| = 5 \times 5$ ground structure) is not better than that in Fig. 9d (for the $|\mathcal{V}| = 4 \times 4$ ground structure). The solution shown in Fig. 15e is same as the one in Fig. 9d; increase of the candidate members in a ground structure does not improve the objective function. The objective value of the solution in Fig. 15f is worse than that in Fig. 15e. Since the instance in Fig. 15f has a large number of design variables, the number of enumeration nodes explored by the MILP solver within 12 h is much less than the other instances. After 48 h run, we obtain the structure shown in Fig. 16. The number of nodes explored by the solver is comparable to the case in, e.g., Fig. 15d. As a result of minor improvements from Fig. 15f, repetitive alignment of V-shape parts is visible in Fig. 16.

We next examine formulation (II). The two ground structures shown in Fig. 17 are used. The structure in Fig. 17a consists of $|\mathcal{V}| = 5 \times 5 = 25$ nodes and $|\mathcal{E}| = 72$ members, and the one in Fig. 17b consists of $|\mathcal{V}| = 6 \times 6 = 36$ nodes and $|\mathcal{E}| = 110$
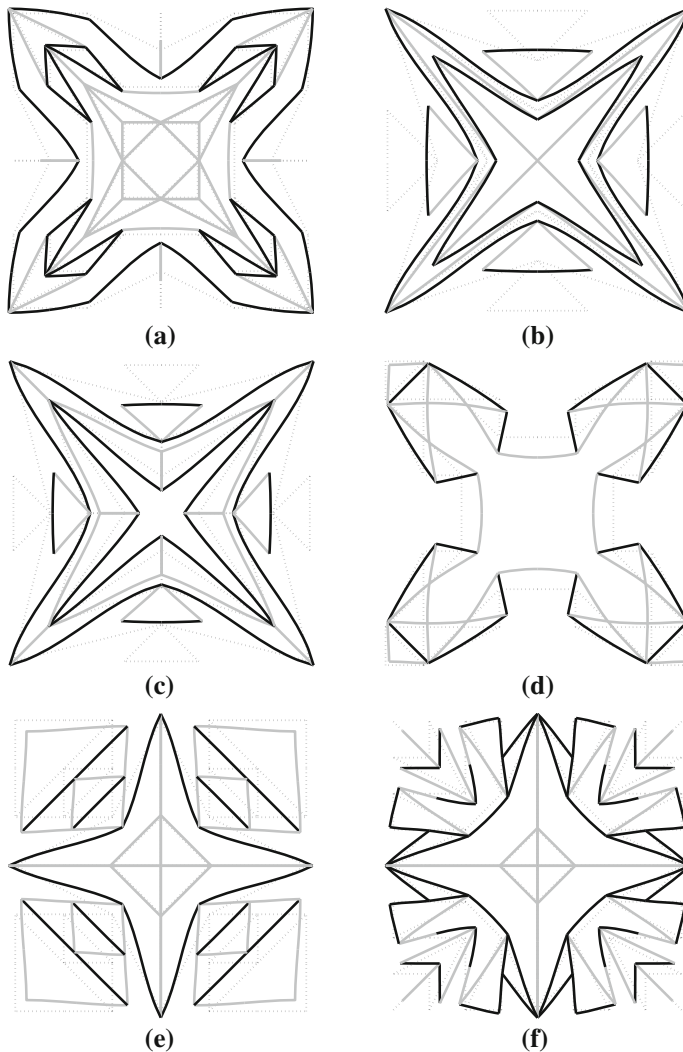
Fig. 15 The best feasible solutions obtained by running the MILP solver for 12 h to solve formulation (I). The solutions for **a** the ground structure in Fig. 14a with pattern (A); **b** the ground structure in Fig. 14b with pattern (A); **c** the ground structure in Fig. 14c with pattern (A); **d** the ground structure in Fig. 14a with pattern (B); **e** the ground structure in Fig. 14b with pattern (B); and **f** the ground structure in Fig. 14c with pattern (B)

members. The computational results are listed in Table 7. The obtained solutions are collected in Fig. 18.

In the solutions shown in Fig. 18a and b, the material with low thermal expansion ($\mathcal{M}_2$) forms a dodecagon with four reentrant corners, that is similar to the exterior structure of the solution in Fig. 11d. In these solutions, the interior structures consisting of the material with high thermal expansion ($\mathcal{M}_1$) are disconnected. The

Fig. 16 The best feasible
solutions obtained by running
the MILP solver for 48 h to
solve formulation (I). The
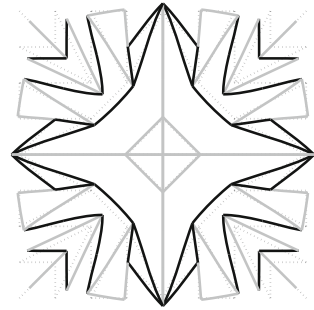solution for the ground structure
in Fig. 14c with pattern (B)

Table 6 Computational results of formulation (I) solved by the heuristic approach. The obtained solutions are shown in Fig. 15

| Ground struct.	Pattern	# of nodes	# of cuts	Gap (mm)	Best obj. (mm)	Time (h)
Fig. 14a	(A)	1,183,797	16	28.0022×10^{-2}	-10.9803×10^{-2}	12.0
Fig. 14b	(A)	7,736,873	20	7.25261×10^{-2}	-15.6511×10^{-2}	12.0
Fig. 14c	(A)	570,653	12	32.9387×10^{-2}	-15.8508×10^{-2}	12.0
Fig. 14a	(B)	2,151,308	17	109.2944×10^{-2}	-1.3948×10^{-2}	12.0
Fig. 14b	(B)	13,172,505	28	23.5387×10^{-2}	-4.6005×10^{-2}	12.0
Fig. 14c	(B)	838,358	16	135.3022×10^{-2}	-3.6957×10^{-2}	12.0
Fig. 14c	(B)	3,314,683	27	111.6910×10^{-2}	-4.1336×10^{-2}	48.0

(a)　　　　　　　　　　　　　　**(b)**
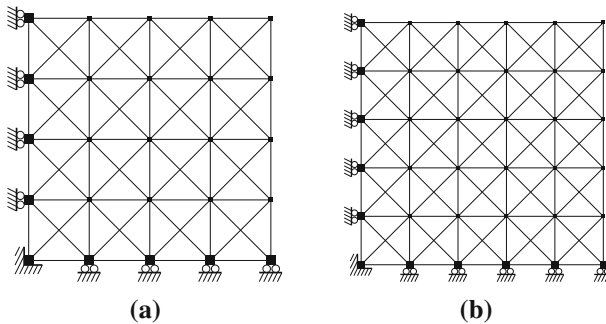
Fig. 17 The ground structures for the heuristic method with formulation (II). The frame structures with **a** $|\mathcal{E}| = 72$ members; and **b** $|\mathcal{E}| = 110$ members

optimal value is improved from the solution in Fig. 11d by using finer ground structures, but the optimal value of the solution in Fig. 18b is no better than the one in Fig. 18a. The solutions in Fig. 18c and d have connected interior structures consisting of $\mathcal{M}_1$. Therefore, bonding between two materials is automatically strengthened by elevation of temperature. Moreover, the solution in Fig. 18d

Table 7 Computational results of formulation (II) solved by the heuristic approach with time limit 12 h. The obtained solutions are shown in Fig. 18

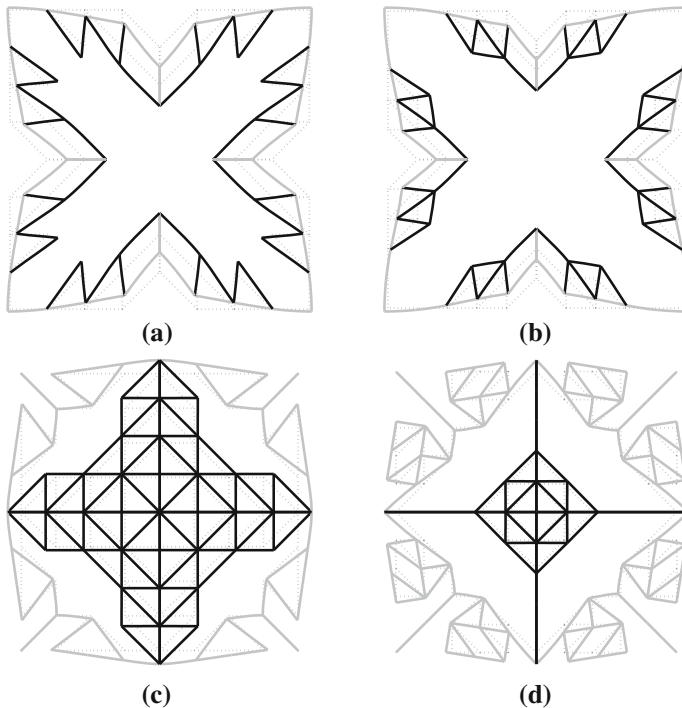| $|\mathcal{V}|$	Pattern	# of nodes	# of cuts	Gap (mm)	Best obj. (mm)
5×5	(A)	1,851,478	168	22.8522×10^{-2}	-7.2319×10^{-2}
6×6	(A)	378,319	243	59.0015×10^{-2}	-7.0805×10^{-2}
5×5	(B)	2,323,876	132	64.7893×10^{-2}	0.2813×10^{-2}
6×6	(B)	419,332	164	174.6725×10^{-2}	-0.1458×10^{-2}

Fig. 18 The best feasible solutions obtained by running the MILP solver for 12 h to solve formulation (II). The solutions for **a** the ground structure in Fig. 17a with pattern (A); **b** the ground structure in Fig. 17b with pattern (A); **c** the ground structure in Fig. 17a with pattern (B); and **d** the ground structure in Fig. 17b with pattern (B)

exhibits a negative thermal expansion property. This is exactly an example of the structures that we attempt to find with the formulation presented in Sect. 4.

6 Conclusions

Materials and structures that exhibit negative thermal expansion have been received significant interest because of their potential applications. This paper has addressed an optimization problem of a planar periodic frame structure, where the

displacement induced by temperature increase is minimized. Numerical experiments showed that periodic frame structures demonstrating thermal contraction can be designed by using two materials with positive thermal expansion coefficients.

The problem dealt with in this paper is considered a three-phase material distribution problem for a given frame structure. Namely, we solve an optimization problem to select the material for each member among from two specified materials and void. In the course of optimization, this material selection is handled by making use of two binary design variables. Also, local stress constraints are fully addressed and existing members have predetermined sections. As a result, the optimal structure obtained by the proposed method has neither hinges nor thin members. In this respect the proposed approach may have an advantage in ease of manufacture of the optimal solution. It is worth noting that solutions with hinge-like regions and/or too thin members often require that, in advance of manufacturing process, thickness of hinges should be adjusted carefully to avoid stress concentration without losing thermal contraction properties.

In this paper the optimization problem has been recast as a mixed-integer linear programming (MILP) problem. Problem instances with relatively small scales can be solved globally with a commercial software package for MILP. Larger instances have been attacked by making use of heuristics already implemented in an MILP solver. Namely, we put maximum time limit that the solver can spend trying to solve an instance and report the best feasible solution. Sometimes such a solution is near optimal and it has been shown that the problems in Sects. 5.1 and 5.2 can be found within 1000 s. Further improvement of the MILP formulation to reduce computational cost could be explored with advanced modeling techniques in integer programming. In this paper we restrict ourselves to finding a structure with the minimum thermal expansion coefficient, where the displacement of the interface node for cell connection, u_1, is minimized. The presented formulation can be extended straightforwardly to a problem finding a structure with a nearly zero thermal expansion coefficient. Namely, we can replace the objective function, u_1, by $|u_1|$. The optimization problem can still be recast as an MILP problem.

In the optimal solution distributions of the two materials can be complicated. With an intricate mixture pattern, a large number of interfaces between two different materials exist in a base cell and many small parts may be required in real manufacturing process. This may cause difficulty in fabrication of a base cell. Section 4 has explored a formulation for avoiding mixture of materials. In this formulation, binary variables are allocated to nodes to determine a material that can be used for each member. Then we consider linear inequality constraints to guarantee that one material is placed only outside of the other one. This formulation, however, limits the solution space excessively. In other words, the formulation excludes several designs with two disjoint material distributions. Also, explicit forms of the linear inequality constraints depend on topology of a ground structure. Hence, for the separation constraints on material distributions, more sophisticated formulations that can express any acceptable solutions remain to be explored.

Concerning negative thermal expansion behavior, this paper has addressed minimization of the displacement of a node that serves as an interface for periodic connection of base unit cells. Two connection patterns have been considered, where

the shape of base cell is supposed to be square. Other shapes of base cell, as well as other connection patterns, remain to be studied. It might be preferable that the connection pattern and the base cell topology are optimized simultaneously. From a practical point of view, issues of geometrical nonlinearity and out-of-plane deformations may possibly have to be considered. Extensions to three-dimensional structures also remain to be explored.

Decomposition of equilibrium equations

According to Kureta and Kanno (2014), we decompose the stiffness matrix, $K(\boldsymbol{E}, \boldsymbol{G})$, in (9b) and (9d). The results obtained below have been used in Sect. 3.1; see (15) and (16).

Consider the local coordinate system for member $e = (i,j) \in \mathcal{E}$ as shown in Fig. 19. The element displacement vector is written as $\hat{\boldsymbol{u}}_e = (u_x^{(i)}, u_y^{(i)}, \theta^{(i)}, u_x^{(j)}, u_y^{(j)}, \theta^{(j)})^\top \in \mathbb{R}^6$. The displacement vector of the whole ground structure, $\boldsymbol{u} \in \mathbb{R}^d$, is defined with respect to the global coordinate system. For each $e \in \mathcal{E}$, transformation of $\boldsymbol{u}$ to $\hat{\boldsymbol{u}}_e$ is written as

$$\hat{\boldsymbol{u}}_e = T_e \boldsymbol{u},$$

where $T_e \in \mathbb{R}^{6 \times d}$ is a constant transformation matrix. We employ the Timoshenko beam theory to model the members of the ground structure. Let $\hat{K}_e(E_e, G_e) \in \mathbb{R}^{6 \times 6}$ denote the member stiffness matrix defined with respect to the local coordinate system. As explained in Kureta and Kanno (2014), $\hat{K}_e$ is given by

$$\hat{K}_e(E_e, G_e) = \sum_{t=1}^{3} k_{et}(E_e, G_e) \hat{\boldsymbol{b}}_{et} \hat{\boldsymbol{b}}_{et}^\top, \tag{45}$$

where $\hat{\boldsymbol{b}}_{e1}, \hat{\boldsymbol{b}}_{e2}, \hat{\boldsymbol{b}}_{e3} \in \mathbb{R}^6$ are defined by

$$\hat{\boldsymbol{b}}_{e1} = \begin{bmatrix} -1 \\ 0 \\ 0 \\ 1 \\ 0 \\ 0 \end{bmatrix}, \quad \hat{\boldsymbol{b}}_{e2} = \begin{bmatrix} 0 \\ -1 \\ -l_e/2 \\ 0 \\ 1 \\ -l_e/2 \end{bmatrix}, \quad \hat{\boldsymbol{b}}_{e3} = \begin{bmatrix} 0 \\ 0 \\ -1 \\ 0 \\ 0 \\ -1 \end{bmatrix} \tag{46}$$

Fig. 19 Local coordinate system for a beam element
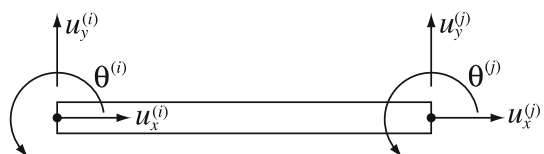
and $k_{e1}, k_{e2}, k_{e3} \in \mathbb{R}$ are defined by

$$k_{e1} = \frac{E_e A_e}{l_e}, \tag{47a}$$

$$k_{e2} = \frac{1}{l_e} \left(\frac{l_e^2}{12 E_e I_e} + \frac{1}{\kappa G_e A_e} \right)^{-1}, \tag{47b}$$

$$k_{e3} = \frac{E_e I_e}{l_e}. \tag{47c}$$

Here, E_e and G_e are Young's modulus and the shear modulus of the beam material, A_e and I_e are the cross-sectional area and the moment of inertia, l_e is length of the beam element, and κ is the shear correction factor in the Timoshenko beam theory. In (47b), we define $k_{e2} = 0$ if $E_e = G_e = 0$ for convention. Note that (46) and (47) correspond to the MacNeal element in the Timoshenko beam theory (MacNeal 1978). In our problem, beams are subjected to nodal loads only. In this case, the MacNeal element coincides with the interdependent interpolation element in Reddy (1997), and hence the nodal displacement of a beam can be predicted exactly with single element (Reddy 1997; Friedman and Kosmatka 1993).

For member $e = (i,j) \in \mathcal{E}$, let $s_e = (s_{e1}, s_{e2}, s_{e3})^\top \in \mathbb{R}^3$ denote the generalized stress vector, which is defined by

$$s_{e1} = q_e, \tag{48a}$$

$$s_{e2} = \tau_e = -\frac{m_e^{(i)} + m_e^{(j)}}{l_e}, \tag{48b}$$

$$s_{e3} = \frac{-m_e^{(i)} + m_e^{(j)}}{2}. \tag{48c}$$

Here, q_e is the axial force, τ_e is the transverse shear force, and $m_e^{(i)}$ and $m_e^{(j)}$ are the two end moments. The force-balance equation in the global coordinate system is then given by

$$\sum_{e \in \mathcal{E}} \sum_{t=1}^{3} s_{et} \boldsymbol{b}_{et} = \boldsymbol{f}, \tag{49}$$

where constant vectors $\boldsymbol{b}_{e1}, \boldsymbol{b}_{e2}, \boldsymbol{b}_{e3} \in \mathbb{R}^d$ are defined by

$$\boldsymbol{b}_{et} = T_e^\top \hat{\boldsymbol{b}}_{et}, \quad t = 1, 2, 3. \tag{50}$$

The generalized stress, s_{et}, is related to the displacement, $\boldsymbol{u}$, as

$$s_{et} = k_{et} \boldsymbol{b}_{et}^\top \boldsymbol{u}, \quad t = 1, 2, 3; \ \forall e \in \mathcal{E}. \tag{51}$$

Since the global stiffness matrix, $K(\boldsymbol{E}, \boldsymbol{G})$, is given by

$$K(\boldsymbol{E}, \boldsymbol{G}) = \sum_{e \in \mathcal{E}} T_e^\top \hat{K}(E_e, G_e) T_e,$$

we can see that elimination of s_{et}'s from (49) and (51) results in the global equilibrium equation

$$K(\boldsymbol{E}, \boldsymbol{G})\boldsymbol{u} = \boldsymbol{f}.$$

Expression in (49) and (51) has served as basis of our MILP formulation.

References

Achterberg T (2009) SCIP: solving constraint integer programs. Math Program Comput 1:1–41

Achtziger W, Kanzow C (2008) Mathematical programs with vanishing constraints: optimality conditions and constraint qualifications. Math Program A114:69–99

Allaire G, Jouve F (2008) Minimum stress optimal design with the level set method. Eng Anal Bound Elem 32:909–918

Barrera GD, Bruno JAO, Barron THK, Allan NL (2005) Negative thermal expansion. J Phys 17:R217–R252

Baughman RH, Galvão DS (1993) Crystalline networks with unusual predicted mechanical and thermal properties. Nature 365:735–737

Bruggi M (2008) On an alternative approach to stress constraints relaxation in topology optimization. Struct Multidiscip Optim 36:125–141

Bruyneel M (2011) SFP–A new parameterization based on shape functions for optimal material selection: application to conventional composite plies. Struct Multidiscip Optim 43:17–27

Chen B-C, Kikuchi N (2001) Topology optimization with design-dependent loads. Finite Elem Anal Des 37:57–70

Chen B-C, Silva ECN, Kikuchi N (2001) Advances in computational design and optimization with application to MEMS. Int J Num Methods Eng 52:23–62

Cheng GD, Guo X (1997) ε-relaxed approach in structural topology optimization. Struct Optim 13:258–266

Deaton JD, Grandhi RV (2013) Stiffening of restrained thermal structures via topology optimization. Struct Multidiscip Optim 48:731–745

Deng J, Yan J, Cheng G (2013) Multi-objective concurrent topology optimization of thermoelastic structures composed of homogeneous porous material. Struct Multidiscip Optim 47:583–597

Duysinx P, Bendsøe MP (1998) Topology optimization of continuum structures with local stress constraints. Int J Num Methods Eng 43:1453–1478

Evans JSO (1999) Negative thermal expansion materials. J Chem Soc Dalton Trans 19:3317–3326

Evans JSO, David WIF, Sleight AW (1999) Structural investigation of the negative-thermal-expansion material ZrW_2O_8. Acta Crystallographica B55:333–340

Friedman Z, Kosmatka B (1993) An improved two-node Timoshenko beam finite element. Comput Struct 47:473–481

Gao T, Zhang W (2010) Topology optimization involving thermo-elastic stress loads. Struct Multidiscip Optim 42:725–738

Gibiansky LV, Sigmund O (2000) Multiphase composites with extremal bulk modulus. J Mech Phys Solids 48:461–498

Gibiansky LV, Torquato S (1997) Thermal expansion of isotropic multiphase composites and polycrystals. J Mech Phys Solids 45:1223–1252

Grima JN, Ellul B, Attard D, Gatt R, Attard M (2010) Composites with needle-like inclusions exhibiting negative thermal expansion: a preliminary investigation. Compos Sci Technol 70:2248–2252

Grima JN, Ellul B, Gatt R, Attard D (2013) Negative thermal expansion from disc, cylindrical, and needle shaped inclusions. Physica Status Solidi (B) 250:2051–2056

Grima JN, Farrugia PS, Gatt R, Zammit V (2007) A system with adjustable positive or negative thermal expansion. Proc Royal Soc A 463:1585–1596

Grima JN, Oliveri L, Ellul B, Gatt R, Attard D, Cicala G, Recca G (2010) Adjustable and negative thermal expansion from multilayered systems. Physica Status Solidi (Rapid Research Letters) 4:133–135

Guo X, Zhang WS, Wang MY, Wei P (2011) Stress-related topology optimization via level set approach. Comput Methods Appl Mech Eng 200:3439–3452

Gurobi Optimization Inc. (2013) Gurobi optimizer reference manual. http://www.gurobi.com/. Accessed October 2013

Holmberg E, Torstenfelt B, Klarbring A (2013) Stress constrained topology optimization. Struct Multidiscip Optim 48:33–47

Hvejsel CF, Lund E (2011) Material interpolation schemes for unified topology and multi-material optimization. Struct Multidiscip Optim 43:811–825

IBM ILOG (2013) User's manual for CPLEX. http://www.ilog.com/. Accessed October 2013

Jacquot P, Lehmann M, Colonna de Lega X (1998) Deformation analysis of a communication telescope structure under non-uniform heating using holographic interferometry. Proc Int Soc Opt Eng 3293:102–113

Jefferson G, Parthasarathy TA, Kerans RJ (2009) Tailorable thermal expansion hybrid structures. Int J Solids Struct 46:2372–2387

Jog C (1996) Distributed-parameter optimization and topology design for non-linear thermoelasticity. Comput Methods Appl Mech Eng 132:117–134

Kanno Y (2013) Topology optimization of tensegrity structures under compliance constraint: a mixed integer linear programming approach. Optim Eng 14:61–96

Kureta R, Kanno Y (2014) A mixed integer programming approach to designing periodic frame structures with negative Poisson's ratio. Optim Eng 15:773–800

Lakes R (1987) Foam structures with a negative Poisson's ratio. Science 235:1038–1040

Lakes R (1996) Cellular solid structures with unbounded thermal expansion. J Mater Sci Lett 15:475–477

Li Y, Saitou K, Kikuchi N (2004) Topology optimization of thermally actuated compliant mechanisms considering time-transient effect. Finite Elem Anal Des 40:1317–1331

Lightfoot P, Woodcock DA, Maple MJ, Villaescusa LA, Wright PA (2001) The widespread occurrence of negative thermal expansion in zeolites. J Mater Chem 11:212–216

Lim T (2005) Anisotropic and negative thermal expansion behavior in a cellular microstructure. J Mater Sci 40:3275–3277

Lim T (2012) Negative thermal expansion structures constructed from positive thermal expansion trusses. J Mater Sci 47:368–373

Lind C (2012) Two decades of negative thermal expansion research: where do we stand? Materials 5:1125–1154

MacNeal RH (1978) A simple quadrilateral shell element. Comput Struct 8:175–183

Martinek C, Hummel FA (1968) Linear thermal expansion of three tungstates. J Am Ceram Soc 51:227–228

Miller W, Mackenzie DS, Smith CW, Evans KE (2008) A generalised scale-independent mechanism for tailoring of thermal expansivity: positive and negative. Mech Mater 40:351–361

Miller W, Smith CW, Mackenzie DS, Evans KE (2009) Negative thermal expansion: a review. J Mater Sci 44:5441–5451

Palumbo NMA, Smith CW, Miller W, Evans KE (2011) Near-zero thermal expansivity 2-D lattice structures: performance in terms of mass and mechanical properties. Acta Materialia 59:2392–2403

Pedersen P, Pedersen NL (2010) Strength optimized designs of thermoelastic structures. Struct Multidiscip Optim 42:681–691

Pedersen P, Pedersen NL (2012) Interpolation/penalization applied for strength design of 3D thermoelastic structures. Struct Multidiscip Optim 45:773–786

Poulsen TA (2003) A new scheme for imposing a minimum length scale in topology optimization. Int J Num Methods Eng 57:741–760

Qi J, Halloran JW (2004) Negative thermal expansion artificial material from iron-nickel alloys by oxide co-extrusion with reductive sintering. J Mater Sci 39:4113–4118

Ramirez AP, Kowach GR (1998) Large low temperature specific heat in the negative thermal expansion compound ZrW_2O_8. Phys Rev Lett 80:4903–4906

Rasmussen MH, Stolpe M (2008) Global optimization of discrete truss topology design problems using a parallel cut-and-branch method. Comput Struct 86:1527–1538

Reddy JN (1997) On locking-free shear deformable beam finite elements. Comput Methods Appl Mech Eng 149:113–132

Rodrigues H, Fernandes P (1995) A material based model for topology optimization of thermoelastic structures. Int J Num Methods Eng 38:1951–1965

Rozvany GIN (2001) On design-dependent constraints and singular topologies. Struct Multidiscip Optim 21:164–172

Sigmund O (2001) Design of multiphysics actuators using topology optimization–Part II: two-material structures. Comput Methods Appl Mech Eng 190:6605–6627

Sigmund O (2007) Morphology-based black and white filters for topology optimization. Struct Multidiscip Optim 33:401–424

Sigmund O, Torquato S (1996) Composites with extremal thermal expansion coefficients. Appl Phys Lett 69:3203–3205

Sigmund O, Torquato S (1997) Design of materials with extreme thermal expansion using a three-phase topology optimization method. J Mech Phys Solids 45:1037–1067

Sleight AW (1998) Isotropic negative thermal expansion. Annu Rev Mater Sci 28:29–43

Steeves CA, dos Santos e Lucato SL, He M, Antinucci E, Hutchinson JW, Evans AG (2007) Concepts for structurally robust materials that combine low thermal expansion with high stiffness. J Mech Phys Solids 55:1803–1822

Steeves CA, Evans AG (2011) Optimization of thermal protection systems utilizing sandwich structures with low coefficient of thermal expansion lattice hot faces. J Am Ceram Soc 94:S55–S61

Steeves CA, Mercer C, Antinucci E, He MY, Evans AG (2009) Experimental investigation of the thermal properties of tailored expansion lattices. Int J Mech Mater Des 5:195–202

Stegmann J, Lund E (2005) Discrete material optimization of general composite shell structures. Int J Num Methods Eng 62:2009–2027

Stolpe M (2007) On the reformulation of topology optimization problems as linear or convex quadratic mixed 0−1 programs. Optim Eng 8:163–192

Stolpe M, Svanberg K (2003) Modelling topology optimization problems as linear mixed 0–1 programs. Int J Num Methods Eng 57:723–739

Theocaris PS, Stavroulakis GE, Panagiotopoulos PD (1997) Negative Poisson's ratios in composites with star-shaped inclusions: a numerical homogenization approach. Arch Appl Mech 67:274–286

Tortorelli DA, Subramani G, Lu SCY, Haber RB (1991) Sensitivity analysis for coupled thermoelastic systems. Int J Solids Struct 27:1477–1497

Wang MY, Wang X (2004) "Color" level sets: a multi-phase method for structural topology optimization with multiple materials. Comput Methods Appl Mech Eng 193:469–496

Wang B, Yan J, Cheng G (2011) Optimal structure design with low thermal directional expansion and high stiffness. Eng Optim 43:581–595

Xia Q, Wang MY (2008) Topology optimization of thermoelastic structures using level set method. Comput Mech 42:837–857

Yoon GH, Kim YY, Bendsøe MP, Sigmund O (2004) Hinge-free topology optimization with embedded translation-invariant differentiable wavelet shrinkage. Struct Multidiscip Optim 27:139–150

Zhou S, Wang MY (2007) Multimaterial structural topology optimization with a generalized Cahn-Hilliard model of multiphase transition. Struct Multidiscip Optim 33:89–111

Zhu B, Zhang X, Wang N (2013) Topology optimization of hinge-free compliant mechanisms with multiple outputs using level set method. Struct Multidiscip Optim 47:659–672